

Understanding Rapid Changes in Phase Partitioning between Cloud Liquid and Ice in Stratiform Mixed-Phase Clouds: An Arctic Case Study

HEIKE KALESSE,^a GIJS DE BOER,^b AMY SOLOMON,^b MARIKO OUE,^c MAIKE AHLGRIMM,^d DAMAO ZHANG,^e MATTHEW D. SHUPE,^b EDWARD LUKE,^f AND ALAIN PROTAT^g

^a *Leibniz Institute for Tropospheric Research, Leipzig, Germany*

^b *Cooperative Institute for Research in Environmental Sciences, University of Colorado Boulder, and NOAA/Earth System Research Laboratory, Boulder, Colorado*

^c *School of Marine and Atmospheric Sciences, Stony Brook University, Stony Brook, New York*

^d *European Centre for Medium-Range Weather Forecasts, Reading, United Kingdom*

^e *Department of Atmospheric Science, University of Wyoming, Laramie, Wyoming*

^f *Environmental and Climate Sciences Department, Brookhaven National Laboratory, Upton, New York*

^g *Bureau of Meteorology, Melbourne, Australia*

(Manuscript received 25 April 2016, in final form 5 August 2016)

ABSTRACT

Understanding phase transitions in mixed-phase clouds is of great importance because the hydrometeor phase controls the lifetime and radiative effects of clouds. In high latitudes, these cloud radiative effects have a crucial impact on the surface energy budget and thus on the evolution of the ice cover. For a springtime low-level mixed-phase stratiform cloud case from Barrow, Alaska, a unique combination of instruments and retrieval methods is combined with multiple modeling perspectives to determine key processes that control cloud phase partitioning. The interplay of local cloud-scale versus large-scale processes is considered. Rapid changes in phase partitioning were found to be caused by several main factors. Major influences were the large-scale advection of different air masses with different aerosol concentrations and humidity content, cloud-scale processes such as a change in the thermodynamical coupling state, and local-scale dynamics influencing the residence time of ice particles. Other factors such as radiative shielding by a cirrus and the influence of the solar cycle were found to only play a minor role for the specific case study (11–12 March 2013). For an even better understanding of cloud phase transitions, observations of key aerosol parameters such as profiles of cloud condensation nucleus and ice nucleus concentration are desirable.

1. Introduction

Observations over the last half century have shown that the Arctic environment has changed at a faster rate than the rest of the planet (Serreze et al. 2009; Hansen et al. 2010). This effect, known as Arctic amplification, reflects the strong positive feedbacks unique to polar regions (Serreze and Barry 2011). Increasing temperatures (Chapman and Walsh 1993; Przybylak 2007; Miller et al. 2013), melting sea ice (Stroeve et al. 2007; Comiso et al. 2008; Comiso 2012), and degrading permafrost

(Romanovsky et al. 2002; Brown and Romanovsky 2008) have all been documented throughout the northern high latitudes. Cloud radiative effects have important impacts on the surface energy budget and melting or growth of land- and ocean-based ice (Kay and Gettelman 2009; Kay et al. 2008; Schweiger et al. 2008), and thus likely play a key role in these changes.

To better understand the causes behind these changes and to help predict the direction of future changes, the scientific community is turning to a variety of numerical modeling tools. These models, while providing interesting insight, have been demonstrated to have issues with the representation of some notable processes. Specifically, simulation of high-latitude clouds has proven troublesome for many models (Tjernström et al. 2008; de Boer et al. 2012, 2014), and in particular correct partitioning of hydrometeor phase (liquid vs ice) has caused issues (Klein et al. 2009; Solomon et al. 2009; Morrison

 Denotes Open Access content.

Corresponding author address: Heike Kalesse, Leibniz Institute for Tropospheric Research, Permoserstr. 15, Leipzig 04318, Germany.
E-mail: kalesse@tropos.de

DOI: 10.1175/MWR-D-16-0155.1

et al. 2011). This phase partitioning is critically important because the two phases impact atmospheric radiative transfer in substantially different ways, with liquid clouds generally being more reflective of solar radiation and more emissive of radiation at infrared wavelengths (Intrieri et al. 2002; Shupe and Intrieri 2004).

One reason these clouds have been so challenging to correctly simulate in numerical models is that their existence and persistence is controlled by ice properties and their interaction with other drivers such as cloud liquid and dynamical forcing (Morrison et al. 2012). The existence of liquid water at supercooled temperatures is inherently unstable due to the fact that liquid water has a higher saturation vapor pressure than ice such that water vapor deposition to ice occurs more readily than to liquid. Because of this, in a mixed-phase environment ice deposition is typically stronger than liquid condensation and often leads to evaporation of liquid (Wegener 1911; Bergeron 1935; Findeisen 1938). From a modeling perspective, this introduces a challenging environment, and models tend to convert water to the ice phase too aggressively (Harrington et al. 1999; Klein et al. 2009), resulting in a shortened lifetime of liquid-containing clouds relative to the true atmosphere. This reduction of simulated cloud lifetime results in excessive incoming solar irradiance at Earth's surface, and reduced incoming longwave (LW) irradiance (English et al. 2015).

To better characterize and understand the partitioning of phase in Arctic clouds, studies have been completed using a combination of surface-based remote sensors. Several previous studies focus on describing phase partitioning in Arctic mixed-phase clouds from a long-term point of view such as a seasonal cycle or interannual variability (e.g., Shupe et al. 2006; de Boer et al. 2009; Shupe et al. 2015) or with an emphasis on spatial differences at multiple Arctic sites (e.g., Shupe 2011). Other studies look at more detailed aspects of the problem, for example on the influence of aerosols or dynamical cloud-surface coupling state or variable surface characteristics on phase partitioning (e.g., Verlinde et al. 2007; McFarquhar et al. 2011; Shupe et al. 2013; Sotiropoulou et al. 2014). Similar aspects have been studied from a modeling perspective (e.g., Fan et al. 2009; Solomon et al. 2011; Fridlind et al. 2012; Ovchinnikov et al. 2014; Savre et al. 2015; Solomon et al. 2015).

On the backdrop of these past studies there is still the need to better understand the interplay of detailed cloud-scale processes with larger-scale processes and how these lead to transitions in phase partitioning. In particular multiscale observational studies are needed to evaluate the general conceptual understanding of these clouds as outlined by Morrison et al. (2012). The current comprehensive study aims to examine processes controlling

phase transitions in a persistent Arctic mixed-phase cloud by using a unique combination of instruments and retrieval methods. It combines observations and models to understand many of the physical processes responsible for changes in phase partitioning and looks at the interplay of large-scale versus local processes.

In this work, the focus is on a persistent low-level single-layer stratiform Arctic mixed-phase cloud observed during 11–12 March 2013 at the U.S. Department of Energy's (DOE) Atmospheric Radiation Measurement (ARM) North Slope of Alaska (NSA) permanent site in Barrow, Alaska (Verlinde et al. 2016). This case is one of particular interest due to a significant shift in observed precipitation that strongly impacted the phase partitioning in the cloud system. For the first 12 h of this case (1100–2300 UTC 11 March), the observed liquid portion of the cloud cover featured a steady cloud-top height (850 m) with a gradually descending liquid cloud base (from 650 to 450 m) and continuous ice precipitation (Fig. 1). At approximately 0000 UTC 12 March the ice precipitation intensity significantly decreased. By 0600 UTC 12 March, a second decrease in precipitation intensity was observed. Thereafter, precipitation was generally light, with some heavier bursts between 0900 and 1400 UTC. By 0900 UTC 12 March, the cloud top had descended to below 600 m and the liquid water amount started to decline. Please note that throughout this manuscript "ice precipitation" is used synonymously with precipitation of ice and snow or simply snowfall.

Through analysis of the data collected by extensive ground-based remote sensing and in situ observing systems (described in section 2a) as well as nested Weather Research and Forecasting (WRF) Model simulations and European Centre for Medium-Range Weather Forecasts (ECMWF) radiative transfer simulations (section 2b), we examine the processes responsible for these rapid changes in precipitation rates and cloud liquid, which ultimately impact the cloud phase partitioning. After introducing the synoptic and mesoscale context in section 3, we evaluate a variety of factors that are necessary to understand phase transitions including the evolution of the internal dynamics and microphysics of the low-level mixed-phase cloud, their response to observed changes in aerosol properties and the mesoscale environment, and the influence of an upper-level cirrus cloud (sections 4 and 5). The conclusions summarizing the findings are provided in section 6.

2. Methods

a. Observations

The U.S. DOE ARM program supports process-level understanding of atmospheric phenomena and the

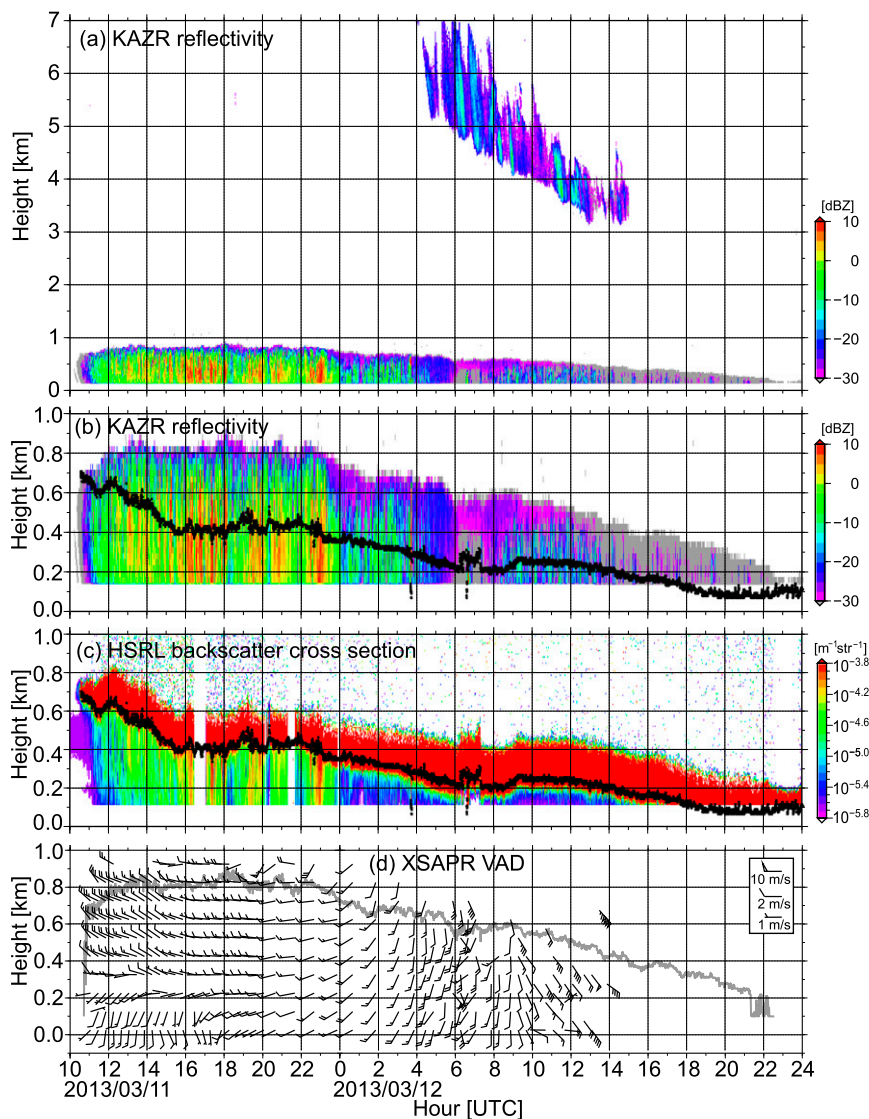


FIG. 1. The stratiform cloud of interest, as seen by the (a) Ka-band radar (KAZR) reflectivity from surface to 7-km altitude, (b) KAZR reflectivity from surface to 1-km altitude, (c) High Spectral Resolution Lidar (HSRL) particle backscatter cross section, and (d) horizontal winds estimated by the VAD method using X-SAPR PPI scans. The VAD method was applied to each PPI scan, and then the estimated horizontal winds were averaged over all PPIs of a volume scan every 50 m and plotted every 100 m. Black dots in (b) and (c) represent cloud bases observed by ceilometer. The gray line in (d) represents the -40 -dBZ isoline of KAZR radar reflectivity.

development of predictive tools through the management and implementation of observational user facilities. The principal NSA facility, along north coastal Alaska, is in Barrow (71.34°N, 156.68°W). This station has been providing key atmospheric measurements to the scientific community since 1997, and includes a wide variety of instrumentation to observe clouds, atmospheric state, surface–atmosphere exchange, and, in collaboration with the National Oceanic and Atmospheric Administration

(NOAA), aerosol particle properties. An overview of the specific instrumentation and data products used in the present study is provided here and summarized in Table 1.

Atmospheric state was obtained from continuous surface meteorological observations of pressure, temperature, relative humidity, wind speed, and wind direction as well as radiosondes launched every 6–12 h. Radiosonde launches were performed at the ARM site

TABLE 1. Instruments with specifications and observed/derived quantities. Abbreviations are explained in the text.

Instrument	Specifications	Observed and/or derived quantities
Weather station sensors		T, p, RH , horizontal wind
Radiosondes	6–12 h	$T, p, \text{RH}, T_d, Q_v$, horizontal wind
Ka-band ARM zenith-pointing radar (KAZR)	35 GHz	Cloud-top height, IWC, $D_{\text{ge}}, N_{\text{ice}}, W, \varepsilon$
High Spectral Resolution Lidar (HSRL)	532 nm	Cloud base, cloud phase, $D_{\text{ge}}, \text{LWC}, R_{\text{eff}}, N_{\text{liq}}$
Microwave Radiometer (MWR)	23.8 and 31.4 GHz	Column-integrated LWP
X-SAPR	Dual-polarization	Horizontal wind profile
TSI 3563 nephelometer	450, 550, and 700 nm	Total scattering and backscattering
Particle Soot/Absorption Photometer (PSAP)	467, 530, and 660 nm	Aerosol absorption
TSI 3010 Condensation Particle Counter (CPC)	10 nm to $3 \mu\text{m}$	Total number concentration of condensation particles

as well as the National Weather Service site in Barrow (approximately 5 km distance; Fig. 2).

An extensive suite of ground-based remote sensing instruments is operated at the Barrow site with High Spectral Resolution Lidar (HSRL) and multifrequency vertically pointing and scanning radars being the key instruments for the observation of clouds and precipitation (Kollias et al. 2007). The synergistic combination of wavelengths observed by these sensors offers a unique opportunity to characterize a variety of cloud, precipitation, and dynamical properties. While radar signals are dominated by larger particles such as ice crystals, lidars are most sensitive to smaller, but more populous, particles such as cloud droplets and aerosol particles (Shupe 2007; Illingworth et al. 2007). This sensitivity of lidars to more abundant smaller particles also results in quicker attenuation, such that these instruments can only penetrate clouds up to an optical thickness of about 3 (Dupont et al. 2010). The full vertical cloud profile above the site is obtained with the 35-GHz Ka-band ARM zenith-pointing radar (KAZR) having a range gate resolution of 30 m and a temporal resolution of 4 s. The KAZR calibration was evaluated using the statistical technique based on *CloudSat* observations (Protat et al. 2011), demonstrating that the KAZR “a1” level datastream is well calibrated. Hydrometeor phase is determined using the HSRL, which measures backscatter intensity and depolarization ratio (Eloranta 2005). High backscatter coefficients and depolarization ratios close to zero indicate cloud regions dominated by liquid phase while regions with high depolarization indicate nonspherical ice crystals (Sassen 2005). Column-integrated values of liquid water path (LWP) are retrieved from microwave radiometer (MWR) measurements (Cadeddu et al. 2013) with uncertainty on the order of 25 g m^{-2} (Westwater et al. 2001) or less.

Microphysical properties of the ice phase [ice water content (IWC), ice particle general effective size D_{ge} (Fu 1996), and ice particle number concentration N_{ice}] and liquid phase [liquid water content (LWC), droplet

number concentration N_{liq} , and droplet effective radius R_{eff}] are retrieved from coincident measurements of HSRL, KAZR, MWR, and radiosondes using advanced multisensor retrieval algorithms (Wang and Sassen 2002; Hogan et al. 2006; Zhang et al. 2014; Wang et al. 2014). Specifically, profiles of D_{ge} are retrieved from HSRL cloud extinction and KAZR reflectivity (Z_e) profiles using algorithms developed in Wang and Sassen (2002). Profiles of IWC are determined using the Z_e -temperature-based IWC retrieval algorithms developed by Hogan et al. (2006). Vertical integration of the IWC results in ice water path (IWP) estimates. The uncertainty in retrieved IWC is approximately 60% based on the evaluations in Heymsfield et al. (2008). The N_{ice} profiles are retrieved from KAZR Z_e measurements using algorithms developed in Zhang et al. (2014) where it was shown that, statistically, the retrieved N_{ice} in stratiform mixed-phase clouds has an uncertainty of a factor of 2. Please note that since N_{ice} is the mean ice particle number concentration between the liquid-dominated mixed-phase layer top and 500 m below, it can only be retrieved if the cloud top is higher than 500 m. LWC profiles are retrieved from cloud liquid-dominated-layer base height and the closest sounding temperature profiles by assuming an adiabatic profile with the integrated LWP constrained by the values retrieved from the MWR. Both N_{liq} and R_{eff} are retrieved from HSRL cloud extinction and LWC profiles (Wang et al. 2014). However, the uncertainties in retrieved N_{liq} and R_{eff} have not yet been evaluated; N_{liq} is only retrieved for $\text{LWP} > 25 \text{ g m}^{-2}$.

In-cloud vertical velocity W and turbulent kinetic energy (TKE) dissipation rate ε are derived from vertically pointing KAZR measurements. Vertical velocity can only be derived in atmospheric parcels that contain cloud liquid water droplets as identified by multiple sensors (Shupe 2007), under the assumption that those droplets serve as tracers for air motions due to their negligible terminal fall speed. The air motion is estimated at the KAZR time resolution of about 4 s using

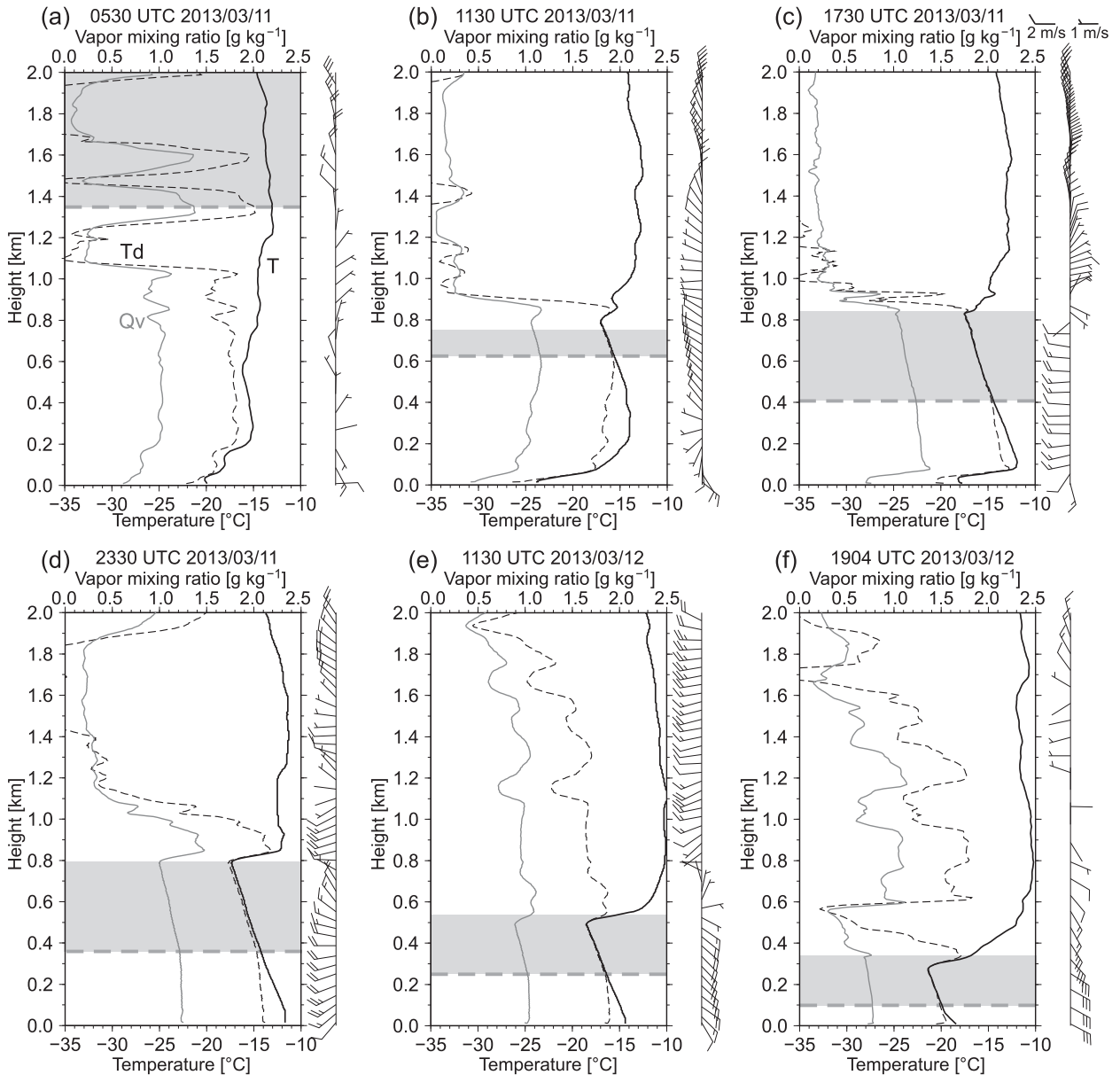


FIG. 2. (a)–(f) Vertical profiles of temperature (black solid line), dewpoint temperature (black dashed line), water vapor mixing ratio (gray solid line), and horizontal winds (barbs) observed by soundings at Barrow. Horizontal gray dashed lines represent liquid-cloud bases observed by ceilometer. Layers between the liquid-dominated cloud base and the highest cloud top estimated from KAZR Doppler spectrum width gradient are represented by gray shading.

the edge of the KAZR Doppler spectra resulting from these liquid droplets (Shupe et al. 2008), with corrections applied for spectral broadening and other biases. For analysis purposes, skewness of the vertical velocity distribution is computed using a running 30-min window over three adjacent vertical heights. The TKE dissipation rate ε is derived from the temporal variance of KAZR mean Doppler velocity for all atmospheric volumes that contain liquid and/or ice hydrometeors (Shupe et al. 2012), under the assumption that variations

of the measured velocity on the time scales of interest are primarily driven by turbulent motions instead of changes in particle terminal fall speed.

Additional insight into the cloud microphysical and dynamical processes is gained by considering higher moments of the KAZR Doppler spectra instead of only the first three moments [reflectivity, mean Doppler velocity, spectral width; Kollias et al. (2007)]. Specifically, the spectral skewness of the primary Doppler spectrum peak (the peak having the highest signal above the mean

TABLE 2. Packages used in the WRF V3.5 Model setup.

Package	Details
Radiation package	National Center for Atmospheric Research Community Atmosphere Model longwave and shortwave radiation package. The longwave code allows for interactions with resolved clouds and cloud fractions (Collins et al. 2004).
Surface layer physics package	Monin–Obukhov with Carlson–Boland viscous sublayer and standard similarity functions following Paulson (1970) and Dyer and Hicks (1970). Surface exchange coefficients for heat, moisture, and momentum computed following Webb (1970). Four stability regimes are defined following Zhang and Anthes (1982).
Land surface package	Noah land surface model; the unified NCEP/NCAR/AFWA scheme with soil temperature and moisture in four layers, fractional sea ice, and snow cover (Chen and Dudhia 2001)
PBL mixing package	Yonsei University scheme with nonlocal- K scheme with explicit entrainment layer and parabolic K profile in unstable mixed layers (Hong et al. 2006)
Microphysics package	Morrison two-moment scheme including prognostic cloud droplets, cloud ice, rain, snow, and graupel/hail (Morrison et al. 2009)

noise level) is analyzed. Pronounced bimodal Doppler spectra (resulting in spectra with nonzero skewness) are an indicator of particles with different fall velocities being present in the same radar sample volume and can be used to identify and characterize liquid- and ice-phase components in mixed-phase clouds (Shupe et al. 2004; Luke et al. 2010; Verlinde et al. 2013; Yu et al. 2014; Kalesse et al. 2016).

To capture the horizontal structure and wind field of the precipitating cloud system, the polarimetric X-band scanning ARM precipitation radar (X-SAPR) was used. The characteristics of the radar system are described in detail in Oue et al. (2016). Plan position indicator (PPI) and range–height indicator (RHI) scans are used here to provide spatial and vertical information on cloud and wind structure. Horizontal wind profiles were estimated using the velocity–azimuth display (VAD) method (Browning and Wexler 1968) applied to X-SAPR Doppler velocities at each elevation angle of the PPI scans.

Surface-based aerosol measurements used in this study are from the NOAA/Earth System Research Laboratory (ESRL) Global Monitoring Division (GMD) Aerosol Observing System at Barrow. This system provides aerosol measurements that are quantitatively comparable to those made at other NOAA and ARM sites, in part due to ARM-funded upgrades in instrumentation in 1997 and 2006. This aerosol observing system provides information on light scattering (TSI Nephelometer) and absorption [Radiance Research Particle Soot/Absorption Photometer (PSAP)] as a function of wavelength for two particle size ranges (>1 and >10 nm). The nephelometer measures total scattering and backscattering at 450, 550, and 700 nm, while the PSAP gives continuous absorption at 467, 530, and 660 nm. In addition, this system obtains information on particle concentration for particles larger than 10 nm

from a TSI 3010 Condensation Particle Counter (CPC). Measurements from these instruments are provided in a quality-controlled format at a temporally averaged resolution of 1 min.

b. Overview of relevant model components

To provide large-scale context for the case and to examine important processes in more detail, multiple model approaches are employed.

Limited-area model simulations are used to identify processes that cause the descent of the cloud layer and the role of surface and large-scale forcing in the observed precipitation and phase partitioning transitions. The limited-area model used is the WRF (version 3.5) with 3 two-way nested grids with horizontal grid spacings (domains) of 12 km ($1176 \text{ km} \times 1176 \text{ km}$), 3 km ($504 \text{ km} \times 504 \text{ km}$), and 0.5 km ($60 \text{ km} \times 60 \text{ km}$) and 46 vertical levels in the lowest 2 km. The model is forced with lateral and surface boundary conditions from the ECMWF four times daily, 137-level, 16-km operational analyses. The model is spun up by integrating from 0000 to 1200 UTC 11 March 2013. The simulations are run from 0000 UTC 11 March to 0000 UTC 13 March 2013. Radiation, surface layer, land surface, and planetary boundary layer options used in the model runs are described in Table 2. Following Morrison et al. (2011) and Ovchinnikov et al. (2014), ice particle formation is parameterized to maintain a constant ice particle number concentration by relaxing to a specified number concentration when the ice supersaturation exceeds 5% and the grid point contains liquid water. The specified total ice + snow particle number concentration used in this study is 1 L^{-1} .

Cloud droplets are activated using resolved and sub-grid vertical motion (Morrison and Pinto 2005) and a lognormal aerosol size distribution (assumed to be ammonium bisulfate and 30% insoluble by volume) to

derive cloud condensation nuclei spectra following [Abdul-Razzak and Ghan \(2000\)](#). The aerosol accumulation mode is specified with concentrations of 200 cm^{-3} , modal diameter of $0.188 \mu\text{m}$, and geometric standard deviation of $1.4 \mu\text{m}$, based on springtime in situ aircraft measurements near Barrow ([McFarquhar et al. 2011](#)). In this formulation, ice nuclei (IN) and cloud condensation nuclei (CCN) are treated as separate species. The microphysical cloud scheme used in this study includes two moments for cloud droplets, rain, ice, snow, and graupel ([Morrison et al. 2009](#)). This means a prognostic equation for mass mixing ratio and number mixing ratio is integrated for each of the five hydrometeor classes.

To estimate the origins of air masses found over the North Slope during this case period, the Hybrid Single-Particle Lagrangian Integrated Trajectory (HYSPLIT; [Draxler and Hess 1998](#)) model was used. HYSPLIT was run online through the Real-time Environmental Applications and Display System (READY; [Draxler and Rolph 2015](#); [Rolph 2016](#)). The simulations completed with HYSPLIT were executed as an ensemble of 24- or 48-h back-trajectory calculations ending in 6-h intervals between 1200 UTC 11 March and 0000 UTC 13 March 2013, with meteorology supplied by the 1° Global Data Assimilation System (GDAS) model from the National Centers for Environmental Prediction (NCEP). Vertical velocity for calculating the trajectories was derived from the model output, and the end point was selected to be at an altitude of 500 m above the Barrow site.

Short-term forecasts from the Monitoring Atmospheric Composition and Climate (MACC) model are used here to gain a wider perspective on aerosol transport at and around the NSA site during the case study period, and help us understand to what degree locally observed shifts in aerosol amount and type might be attributed to advection versus local processing. A lower-resolution version (T255, 60 level) of the operational ECMWF model has been developed under the MACC project to include 12 aerosol species ([Morcrette et al. 2009](#); [Benedetti et al. 2009](#)). The model is primarily a chemical transport model: sources are prescribed at the surface, but the vertical distribution is largely determined by the model transport. Observed Moderate Resolution Imaging Spectroradiometer (MODIS) total aerosol optical depth (AOD) is assimilated by the MACC system and acts as a constraint on total aerosol amount. However, the assimilation system does not change the relative contribution to total AOD by each individual aerosol species, but adjusts the mass in all categories in proportion to achieve a better match to the observed total AOD. Wet removal by precipitation is included, but the aerosol is otherwise noninteractive with the microphysics and radiation. As such, the details

of speciation may be unreliable at times, but to the degree that the model captures the air motion well, it can provide reasonable constraint on the larger-scale transport of air masses and some basic aerosol properties contained therein.

Finally, an offline version of the operational ECMWF forecast model's radiation scheme ([Morcrette et al. 2008](#)) is used to gain a better understanding of the potential radiative impact of the observed clouds. The scheme uses the Rapid Radiative Transfer Model ([Mlawer et al. 1997](#)) in conjunction with the Monte Carlo independent column approximation ([Barker et al. 2002](#); [Pincus et al. 2003](#)) for both shortwave and longwave calculations. To this end, the ECMWF offline radiation model is used for single time steps with prescribed profiles for atmospheric and cloud variables. The starting points for these profiles are the operational model profiles from the grid point nearest the NSA site, which are close to the observed profiles from radiosonde due to data assimilation. The model's cloud variables (LWC, IWC, and cloud fraction) are then replaced with estimated hourly mean values from retrievals performed on the observations (see [section 2a](#)).

3. Synoptic and mesoscale context

The cloud system of interest for this case, as revealed by KAZR and HSRL measurements at Barrow, consisted of a low-altitude, mixed-phase stratocumulus cloud observed from 1100 UTC 11 March to 2400 UTC 12 March ([Fig. 1](#)). Throughout the period of interest, the NSA site was influenced by a high pressure system centered east of Barrow and moving slowly eastward. Regional MODIS satellite imagery (not shown) reveals a fractured sea ice pack with typical lead patterns in the ice associated with deformation to the north and west of Barrow. Along the coast to the southwest of Barrow there was open water area extending 5–20 km offshore that could serve as a source of moisture and heat to the lower atmosphere.

The temporal and spatial structure of horizontal winds during the case was observed from periodic radiosondes providing high-resolution vertical profiles ([Fig. 2](#)) as well as consistent measurements by surface anemometers ([Fig. 3b](#)) and vertical profiles from X-SAPR measurements using the VAD technique ([Fig. 1d](#)). X-SAPR PPI scans were used to estimate spatial distributions of low-level winds as well as cloud and precipitation structures ([Fig. 4](#)).

Prior to the onset of the stratocumulus cloud at Barrow surface layer winds were easterly, with generally weak vertically incoherent winds below 1 km ([Fig. 2a](#)). When the cloud layer initially appeared at Barrow

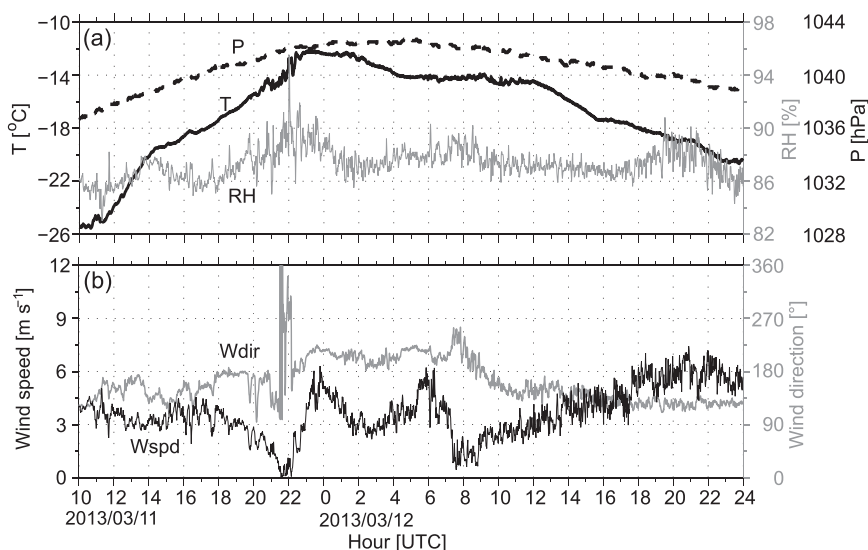


FIG. 3. Surface meteorological conditions for the period of interest: (a) surface pressure (P , dashed), surface air temperature (T , black solid), and relative humidity (RH , gray); and (b) wind direction ($Wdir$, gray) and wind speed (black solid).

around 1030 UTC 11 March, surface layer winds were southeasterly, with substantial shear in the lowest 300 m and primarily west-northwest winds up through the cloud level and into the free troposphere (Figs. 1d and 2b). To the west of Barrow was a region of west-southwesterly low-level winds that approached in time (Fig. 4). At 1639 UTC the X-SAPR PPI showed large-scale, low-level convergence near Barrow leading to isentropic ascent. At about 2300 UTC 11 March a weak mesoscale boundary with warm front characteristics passed over Barrow from the west. This frontal passage resulted in a further shift to southwesterly surface layer winds, with closer alignment to the descending layer of westerly cloud level winds, and decreased vertical shear. Over the following hours the cloud level winds shifted more southerly, then around 0800–0900 UTC 12 March, the winds from the surface up through the cloud level all shifted toward a southeasterly direction and steadily increased in strength through the end of the case (Figs. 1d and 4).

The large-scale setting and resulting winds strongly influenced the atmospheric thermodynamic structure within which the clouds of interest occurred. Before the low cloud encroached upon Barrow, radiosonde and surface meteorological measurements show cooling surface temperatures below -20°C , a near-surface temperature inversion, and water vapor mixing ratios Q_v at or less than 1.0 g kg^{-1} (Fig. 2). At 1130 UTC, shortly after the cloud formed near solar midnight, warm westerlies above 100 m and low surface temperatures initially strengthened the near-surface temperature

inversion. At this time, a cloud-top inversion at about 800 m was also observed. In time the near-surface inversion weakened as the westerly winds aloft descended down toward the surface thus deepening the mixed-layer from above. This process in combination with low-level warm air advection from the open lead to the southwest of Barrow, cloud radiation, and solar insolation warmed the surface layer. Over this time, increases in water vapor mixing ratio at cloud level supported further cloud formation. By the 1730 UTC sounding (near local sunrise), the cloud was 400 m thick, with a strengthening cloud-top inversion, and a well-established cloud-driven mixed-layer extending down to 100 m above the surface. The surface layer below the cloud-driven mixed layer remained relatively dry, and subsaturated with respect to ice, throughout most of 11 March. By the time of the passage of the mesoscale boundary with warm front characteristics (around 2300 UTC 11 March), surface temperatures had risen to -12°C coinciding with solar noon (Fig. 3a). At this transition the cloud-driven mixed layer became coupled to the near-surface with a very thin isothermal surface layer of a few tens of meters remaining through a combination of cloud-driven mixing of relatively warm air downward, near-surface winds shifting toward the southwest, and cloud and solar radiative effects warming the surface. The cloud layer at this time was maintained by water vapor mixing ratios of $1.2\text{--}1.5\text{ g kg}^{-1}$, potentially supported at low levels by the southwesterly flow over the open water near Barrow, and a cloud-top moisture inversion that likely supported cloud persistence (e.g., Solomon et al. 2014). Over the

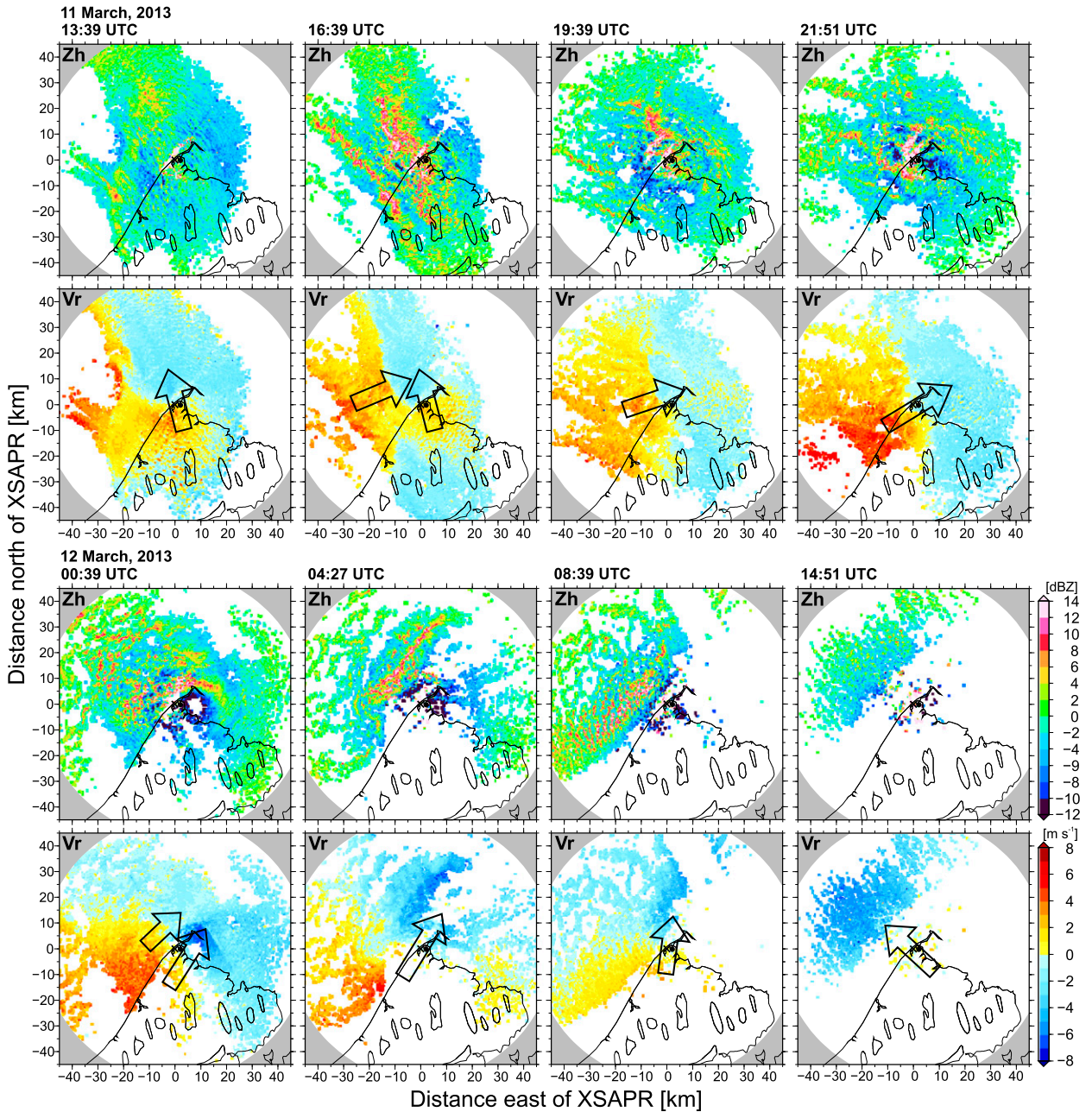


FIG. 4. Time series of X-SAPR reflectivity (labeled Zh) and Doppler velocity (labeled Vr) from PPI measurements at an elevation angle of 0.5° . Cross and dot marks in each panel represent locations of X-SAPR and KAZR, respectively. Large arrows in the Doppler velocity panels represent general wind directions estimated from the Doppler velocity measurements.

following day, the cloud-driven mixed layer remained coupled to the near surface while the water vapor supply, cloud temperature, and surface temperature all decreased as cloud-level winds shifted toward southerly and then southeasterly directions. All of these trends contributed to the descent and thinning of the cloud. Additionally, the ECMWF analysis indicates subsiding large-scale vertical motion within and just above the

boundary layer throughout most of the period considered. In the absence of sufficient entrainment or horizontal convergence in the boundary layer, the subsidence will contribute to a lowering of the cloud top. During 12 March while the cloud was thermodynamically coupled to the near surface, the cloud top extended into the temperature inversion as reported in previous studies (e.g., Sedlar et al. 2012).

A second cloud layer was observed over Barrow starting at 0400 UTC 12 March. This cirrus cloud appears to result from a synoptic-scale occluded warm front advected by north-northwesterly winds aloft. The ice cloud descended over time (cloud base decreasing from 5 to 3 km; Fig. 1a). The lifting process aloft diminished gradually resulting in the dissipation of the cirrus at around 1500 UTC 12 March.

4. Evolution of cloud properties and phase partitioning

a. Macrophysics including major shifts in precipitation

During the 37-h duration of the mixed-phase cloud over Barrow, substantial temporal variability in the liquid-cloud layer and associated ice precipitation was observed. For the first third of the case (1100–2300 UTC 11 March), the cloud top was relatively constant at 850 m (Fig. 1b). During the first 5 hours that the cloud appeared over Barrow, the cloud base descended from 650 to 400 m (Fig. 1c), the total cloud thickness increased, and the LWP increased from 0 to 80 g m^{-2} (Fig. 5a). IWP also increased during this time from 0 to nearly 100 g m^{-2} (Fig. 5b). Thereafter, until about 2300 UTC 11 March the layer thickness remained approximately steady with LWP varying between 40 and 100 g m^{-2} (mean of 70 g m^{-2} , Fig. 5a) and persistent ice precipitation with IWP varying between near 0 to 150 g m^{-2} (mean of 40 g m^{-2} ; Fig. 5b). The strongest ice precipitation was observed at 1600–1800 UTC 11 March followed by several snow showers until 2300 UTC. Over this time the ice ratio, defined as $\text{IWP}/(\text{LWP} + \text{IWP})$, varied between 0 and 0.8 (mean of 0.4; Fig. 5c). At about 2300 UTC 11 March, with the passage of the local front, two important transitions occurred in the cloud structure. First, ice production and precipitation declined sharply, with IWP values less than 10 g m^{-2} (Fig. 5b) and ice ratios typically much less than 0.2 (Fig. 5c). Second, until about 0700 UTC 12 March, the cloud top descended in two steps down to about 600 m, with LWP remaining variable but within the $30\text{--}90 \text{ g m}^{-2}$ range (mean of 65 g m^{-2}). After 0800 UTC 12 March a second transition occurred, which started the dissipation phase of the cloud layer. Over time the cloud top descended steadily and LWP slowly declined toward complete cloud dissipation over the following 16 h (Fig. 5a). Time–height evolution of retrieved IWC and LWC are shown in Figs. 5f and 5g, respectively.

The regional structure of the precipitating clouds as it relates to the general wind field is revealed in Fig. 4. Snowbands extending from northwest to southeast are

indicated by areas of high reflectivity (Fig. 4). The snowbands passed through Barrow from west to east until 0000 UTC 12 March. The strongest snowfall ($0.3\text{--}0.4 \text{ mm h}^{-1}$) occurred at 1600–1800 UTC (Fig. 4, 1639 UTC). After 1800 UTC 11 March there were some intermittent snow showers due to decreased stability aloft until 2300 UTC (Fig. 4; 1939 and 2151 UTC). Afterward, snowfall intensity decreased. The X-SAPR PPI measurements reveal that the intermittent snow showers then became associated with scattered stratocumulus cloud streets. These cloud streets developed near Barrow as the result of cold dry air flowing from over a cold ice- and snow-covered land surface to over a warmer open water surface, initiating a surface-driven convective boundary layer. Directly after the frontal passage, these clouds reached the Barrow shoreline, but with winds shifting to south-southwesterly on early 12 March they moved predominantly offshore (Fig. 4; 0427 and 0839 UTC). A second decrease in ice precipitation was observed at around 0400 UTC 12 March, coinciding with the detection of the upper-level cirrus clouds over the Barrow site.

b. Microphysical evolution

Figure 5d shows the temporal evolution of liquid-dominated layer mean cloud droplet number concentration N_{liq} and ice particle concentration N_{ice} as retrieved from surface-based remote sensors. The N_{liq} fluctuated between 50 and 350 cm^{-3} with a mean of 170 cm^{-3} until 0400 UTC 12 March, then decreased sharply to 80 cm^{-3} and remained low until 0700 UTC 12 March. After this time there was a sharp increase to 300 cm^{-3} . The retrieved N_{ice} remained almost unchanged with values of $1\text{--}10 \text{ L}^{-1}$ until 0000 UTC 12 March, then it dropped sharply to approximately 0.1 L^{-1} , followed by another drop at 0600 UTC 12 March down to approximately 0.01 L^{-1} . These two times of sharp decrease of N_{ice} correspond to the times of ice and precipitation reduction as seen in Fig. 5f. Considering also the temporal evolution of layer-mean D_{ge} (Fig. 5e), which decreased from values of up to $200\text{--}100 \mu\text{m}$ at 0000 UTC 12 March and then at 0400 UTC 12 March started to drop to $20 \mu\text{m}$, it can be concluded that the sharp decreases of IWC (and IWP) may be caused by decreases in both N_{ice} and D_{ge} .

The evolution of skewness of the KAZR Doppler spectrum (s_D) is shown in Fig. 5h. As previously mentioned, s_D is nonzero if multiple hydrometeor populations with different fall velocities are present in the same KAZR sampling volume. With negative velocities indicating downward motion, a *negative* skewness indicates that the slower particle mode dominates the radar return while a *positive* skewness results when the

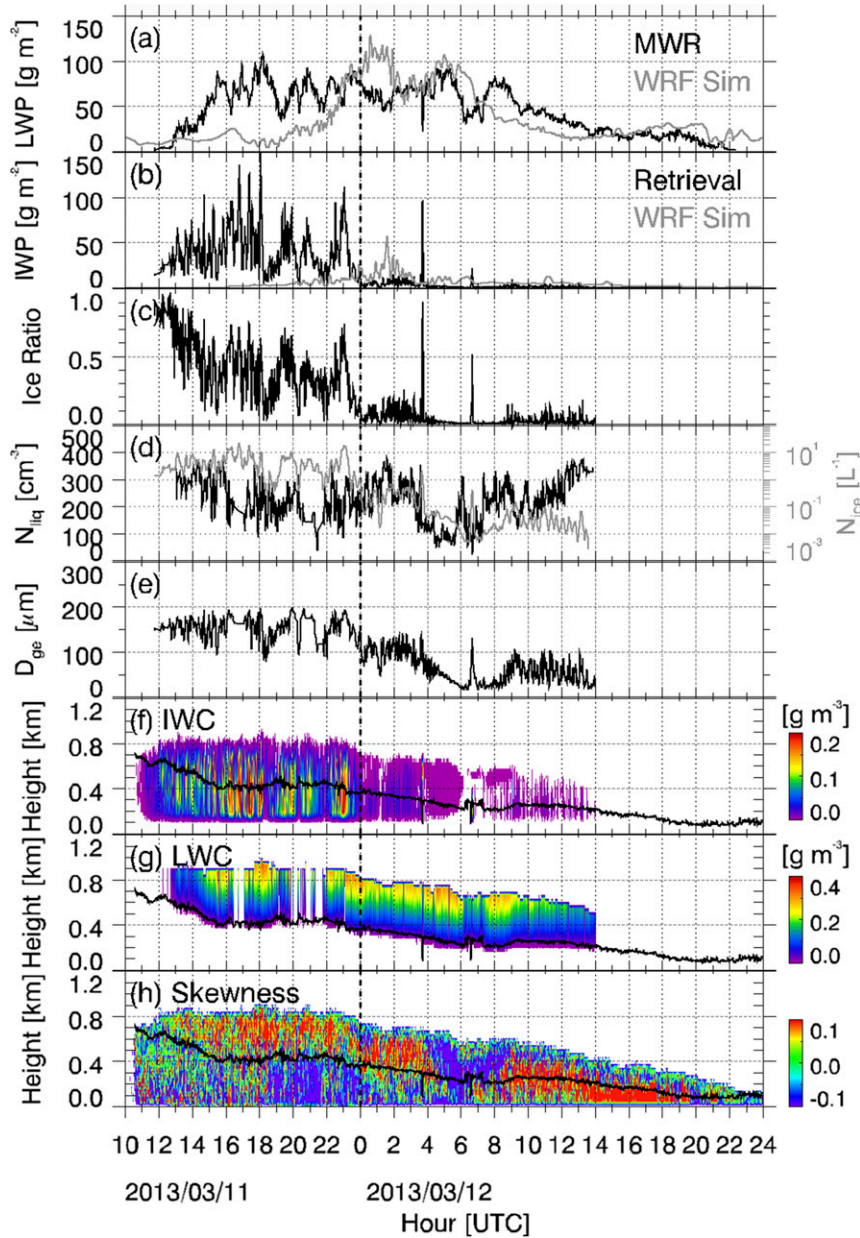


FIG. 5. Time series of (a) MWR-derived LWP (black) and WRF-simulated LWP (gray), (b) retrieved (black) and WRF-simulated (gray) IWP, (c) retrieved ice ratio, (d) retrieved N_{liq} (black) and N_{ice} (gray), (e) retrieved layer-mean D_{ge} , (f) retrieved IWC, (g) retrieved LWC, and (h) KAZR Doppler spectra skewness s_D . The black line in (f)–(h) represents the liquid-cloud base observed by the ceilometer.

backscatter of the faster falling particle mode exceeds that of the slower mode. At cloud top, where LWC is highest, negative skewness was observed while within the cloud skewness was mostly positive due to the growing influence of ice precipitation on the KAZR Doppler spectrum. Below liquid base the skewness was near neutral until 1800 UTC 11 March. Strong negative s_D in the subcloud at 1800–2400 UTC 11 March indicates

multiple ice precipitation modes. Radiosondes indicate that temperatures in the liquid-dominated part of the cloud were -16° to -14°C , a temperature range where dendrites are formed (Fukuta and Takahashi 1999). KAZR Doppler spectra analysis (not shown) suggests that the negative s_D signature is caused by pure dendrites falling at a few tens of centimeters per second and (fewer) larger ice particles falling at up to

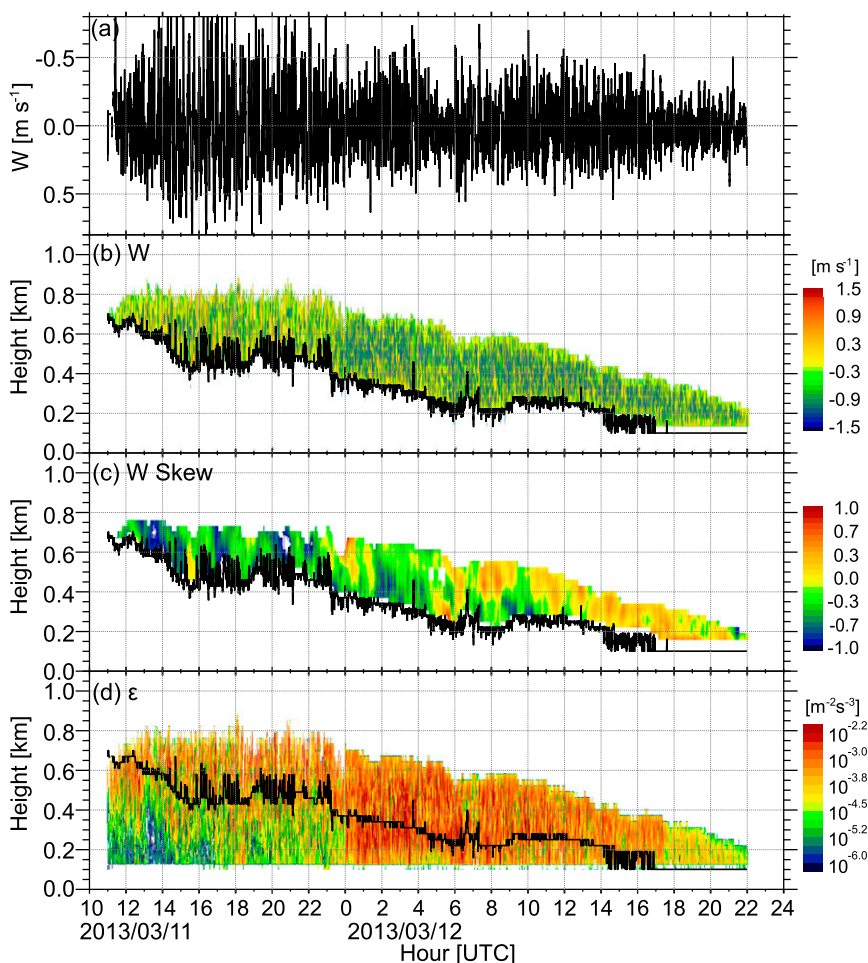


FIG. 6. (a) Time series of layer-mean-retrieved W , and time-vs-height cross sections of (b) W above the liquid-dominated cloud base, (c) skewness of W , and (d) turbulent kinetic energy dissipation rate ϵ . The black line in (b)–(d) represents the liquid-dominated cloud base observed by the ceilometer.

1.3 m s^{-1} . According to Fukuta and Takahashi (1999), riming growth at around -15°C is not expected, especially in an environment of rather low LWP of $50\text{--}100 \text{ g m}^{-2}$. The larger ice particles are thus likely aggregates of dendrites. The X-SAPR-observed differential reflectivity averaged over low elevation angles showed low values of less than 0.8 dB , suggesting that spatial particles dominated in the precipitation. Both the ceilometer (pointing 1° off zenith, not shown) and the HSRL (pointing 4° off zenith) show regions of increased particle backscatter cross section below cloud base at $1800\text{--}2400 \text{ UTC}$ 11 March, which also is an indicator of increased total surface area of precipitating particles during the time of stronger ice precipitation. At 0400 UTC 12 March s_D changed to negative values throughout the entire vertical column from cloud top to the lowest radar range gate. This change from positive to negative in-cloud s_D is consistent with very

limited ice production and ice mass; supercooled liquid droplets thus dominated s_D throughout the entire cloud from around 0400 to 0900 UTC . After this time, weak ice production started again and the droplets only dominated at cloud top. This is in agreement with retrieved D_{ge} , which increased again to about $50 \mu\text{m}$ at this time.

c. Local cloud dynamics

Retrievals of vertical air motions and turbulent dissipation rates (Fig. 6) show that the cloud environment underwent an important dynamical transition at 0000 UTC 12 March, concurrent with the frontal passage, decrease in precipitation, and descent of the liquid cloud base. In particular, the vertical profile of turbulent dissipation rate (Fig. 6d), which is a proxy for the magnitude of turbulent mixing, suggested that before this transition the strongest turbulent mixing was associated with the

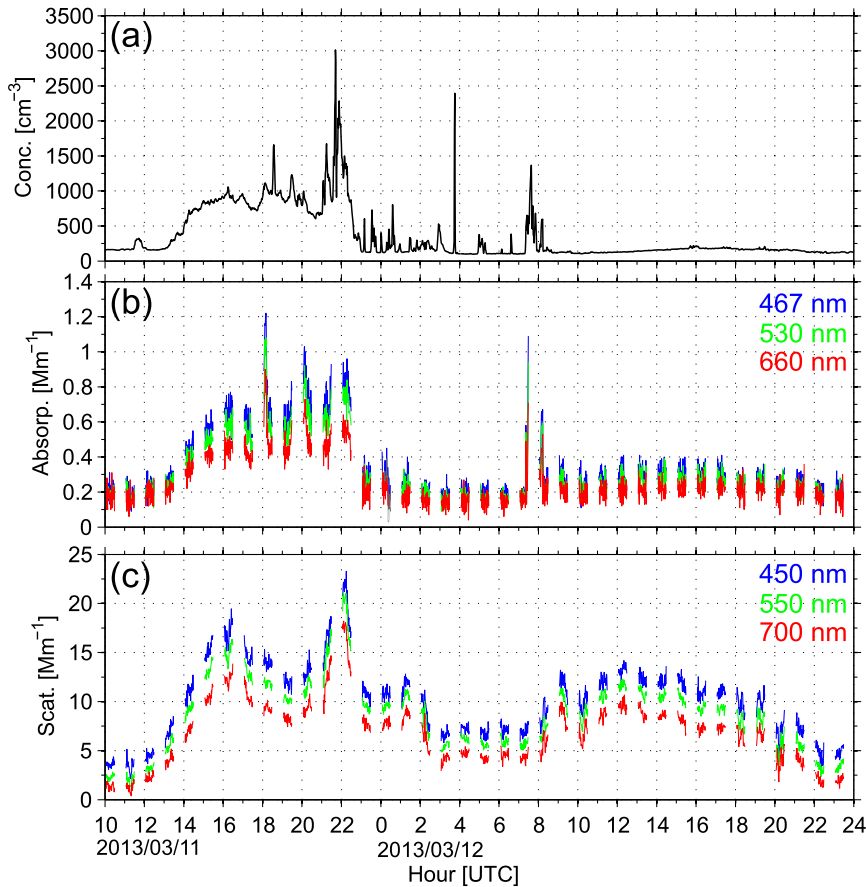


FIG. 7. Surface aerosol properties observed at Barrow. Included are (a) particle concentration for particles larger than 10 nm (TSI 3010 CPC), (b) aerosol absorption (PSAP), and (c) aerosol scattering (TSI nephelometer).

cloud and did not reach down to the surface (i.e., the cloud was dynamically decoupled from the surface). After the transition, the dissipation rate values suggest that significant turbulent mixing extended from the cloud down to the lowest radar gate (105 m), indicating that the cloud and near-surface were coupled. The amplitude of layer-mean vertical velocity also decreased when this coupling state changed (Fig. 6a). Skewness of vertical velocity (s_w), which provides information on the relative partitioning between downdrafts and updrafts, was initially strongly negative, indicating stronger, narrower downdrafts (Fig. 6c). Starting at 0000 UTC 12 March, s_w became increasingly more positive indicating a transition toward relatively stronger, narrower updrafts. This suggests a transition in the relative forcing for vertical mixing from cloud-top radiative cooling toward lower level and/or surface processes as the cloud became coupled to the near surface and the cloud base descended (e.g., Shupe et al. 2013). This shift in dynamical structure is consistent with the observed changes in thermodynamic structure and

the shift toward cloud streets observed after the frontal passage.

d. Aerosol properties

Evaluation of the aerosol properties observed at the surface indicates that before 1300 UTC 11 March, the aerosol concentration was consistently around 200 cm^{-3} (Fig. 7). At 1300 UTC 11 March just after the cloud layer encroached, the air mass at Barrow became substantially more polluted, with aerosol concentrations increasing to around 1000 cm^{-3} with short periods with higher values, including peak concentrations of $1500\text{--}3000 \text{ cm}^{-3}$. The presence of polluted air is further supported by an increase in absorption during this time, indicating an elevated amount of carbonaceous aerosol transported from lower latitudes. After the frontal passage at 2300 UTC 11 March, the aerosol concentrations drop rapidly to values around $200\text{--}300 \text{ cm}^{-3}$. A spike in aerosol concentration at 0720–0815 UTC is associated with a surface-level wind shift toward the west-southwest. Based on the corresponding increase in

absorption (Fig. 7b) during this time, this is likely the result of local (i.e., Barrow) pollution reaching the site. Interestingly, while both the concentrations and absorption appear to return to their background values after the polluted air moved out of the area, aerosol scattering (Fig. 7c) remained elevated relative to its valued prior to 1200 UTC 11 March.

These local aerosol observations can be put into context with the wider flow by considering HYSPLIT back trajectories and the aerosol burden from the MACC forecast. Total aerosol depth (AOD) at 500 nm from the short-range MACC model forecast (initialized at 0000 UTC 11 March and integrated for 48 h, not shown) indicates a polluted air mass to the west and south of Barrow on 11 March. Over the period of interest, the air mass slowly moves east toward Barrow, while the region with elevated AOD to the south retreats farther south.

Back trajectories ending at 1200 UTC 11 March initially group into three clusters with near-surface trajectories generally originating in the east and south, while ones advected from higher altitudes (0.5–1 km) originate in the southwest and west where the MACC forecast suggests higher AODs. By the end of 11 March, most trajectories originate in the (polluted) west and southwest, and the origin of most trajectories is above 0.5 km. Throughout 12 March, increasingly more trajectories arrive at the site from a south-southeasterly direction where the MACC forecast indicates a cleaner air mass.

Together with the direction of the low-level flow (Fig. 3b) this suggests that the higher levels of observed surface aerosol concentration on 11 March may indeed be due to the advection of polluted air (from the west) that diminishes early on 12 March due to a shift in low-level airflow to a more southeasterly direction, a region of origin where the aerosol load is decreasing over time. The MACC forecast itself is consistent with this interpretation, showing a decrease in individual MACC aerosol species' mixing ratios in the near-surface layers during 12 March.

5. Understanding phase transitions

The numerous observational and modeling resources are brought together to understand the processes that control the cloud phase partitioning and its transition in time for this case. This section explores the details of the case that might explain the transition in phase including influences on atmospheric structure, advection, aerosols, and radiative processes. Specifically, we focus on the interplay of local, cloud-scale processes and the large-scale environmental forcing.

The general situation can be summarized as follows: initially, on 11 March the Arctic mixed-phase cloud formed from moisture advected aloft from westerly directions while the cloud is dynamically decoupled from the surface. The surface aerosol concentration increased as ice precipitation began to reach the surface and aerosol properties aloft appear to have allowed for continuous ice production.

Toward the end of 11 March, the low-level wind direction changed to southwest so that the local open ocean could have acted as an additional low-level moisture supply during the time of stronger ice precipitation linked to a frontal system. After the frontal passage (2300 UTC 11 March–0000 UTC 12 March), a change in air mass, especially at low levels, modified the thermodynamic environment, leading to a cloud–surface coupled state and a dramatic drop in ice precipitation rate. At the same time, a change in surface aerosol concentrations and properties was observed. The broader features of aerosol concentration (Fig. 7) and retrieved IWP of the mixed-phase cloud (Fig. 5) are well correlated. This suggests that aerosol properties aloft likely also changed, leading to a decrease in ice formation, a change that is substantiated by a MACC model forecast showing cleaner near-surface levels that may be associated with a reduction in IN. We additionally speculate that it is possible that IN recycling—the reactivation of IN that are mixed vertically by turbulent processes after sublimation in the drier subcloud layer—may have contributed to maintaining high IWP in the decoupled state (before 0000 UTC 12 March) while this process did not play a role after the transition to a near-surface-coupled state when precipitating ice falls in a moisture-rich environment down to the surface and is thus not available for recycling as found in previous studies (e.g., Solomon et al. 2015; Yang et al. 2015). The depth of the mixed-phase layer—which also influences ice particle residence time and thus depositional growth—does not show a significant decrease concurrent with the strong decrease in IWP at 2300 UTC 11 March. Instead, it decreased from 400 to 300 m at 0000–0200 UTC 12 March and then increased again to 350–400 m.

Over the course of 12 March, surface- as well as in-cloud temperature and water vapor content decreased contributing to cloud descent and thinning during a wind shift to first more southerly and later more southeasterly directions. With all else being constant, this cooling of the cloud layer would typically result in an increase in ice production, and not the observed decrease. Therefore, the decrease in ice production does not appear to be the direct result of the evolving thermodynamic regime associated with this system but rather a shift in aerosol. Interestingly, cloud LWP was maintained during the

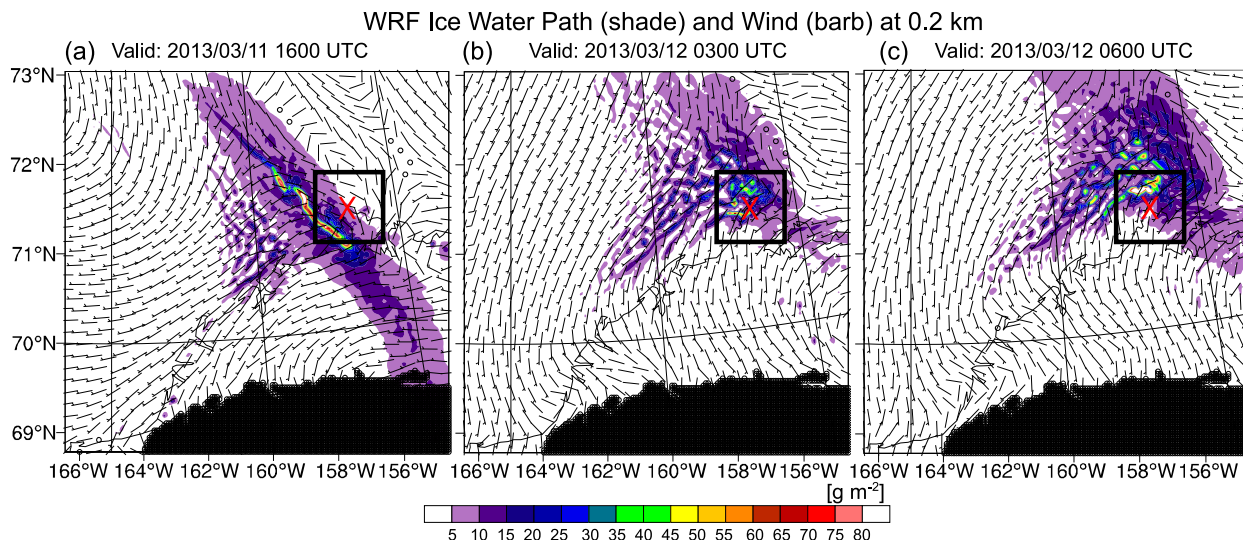


FIG. 8. Horizontal cross sections of ice water path (IWP, color shades) and horizontal wind (barbs) at 0.2-km altitude from the 3-km nest WRF simulations for (a) 1600 UTC 11 Mar, (b) 0300 UTC 12 Mar, and (c) 0600 UTC 12 Mar. IWP in units of g m^{-2} , short barbs indicate 5 m s^{-1} , and long barbs indicate 10 m s^{-1} . The crisscross mark and rectangular region in each panel represent the location of Barrow and the X-SAPR observation region presented in Fig. 4, respectively.

transition to a near-surface coupled state and only decreased when the direction of air mass advection shifted to southeast, suggesting a reduction of CCN concurrent with the advection of a drier and cleaner air mass. The overall decrease in total water (cloud plus vapor) in time appears to be primarily controlled by advection as the ice precipitation was too weak to be a significant sink of moisture.

To get additional insight into the cloud evolution, WRF Model simulations were performed. For model validation, we first examine the ability of the WRF Model simulations to produce cloud fields similar to those observed. Figure 8 displays spatial distributions of IWP and horizontal wind at 0.2-km height from the 3-km WRF nest, which are similar to the X-SAPR measurements (Fig. 4). Specifically, the main features of the observed cloud system are well represented, including the band of high IWP at 1600 UTC 11 March in Fig. 8a, and the subsequent regions of scattered stratocumulus cloud streets with relatively high IWP located near Barrow (Fig. 8b), which then moved predominantly offshore as winds shifted to the south on 12 March (Fig. 8c).

To evaluate WRF Model-simulated vertical structure, time–height cross sections of simulated cloud + snow ice water content, cloud liquid water content, and wind direction from the 0.5-km WRF nest at Barrow are displayed in Fig. 9. WRF simulation results show a liquid-topped mixed-phase cloud with a pronounced evolution of cloud-top, liquid-cloud base, and ice precipitation intensity. Before 2300 UTC 11 March, simulated

IWC was relatively low ($0.005\text{--}0.01 \text{ g kg}^{-1}$), while cloud top increased with time from 0.4 to 0.9 km (Fig. 9b). With values up to 0.05 g kg^{-1} , the simulated IWC peaked between 2000 and 0300 UTC 12 March, which is approximately 5 h later than observed by radar at Barrow (Figs. 4 and 5f). During that period modeled LWC also had maximum values. Simulated temperature and wind direction (Fig. 9c) reveal that the modeled snowbands are consistent in time with warm and moist advection by southwesterly winds below 0.4 km. After the snowband passage, ice precipitation and cloud-top height both decreased, with the ice eventually ceasing altogether while the cloud liquid persisted longer. These features generally correspond to what the observations showed. Thus, even though the timing is not correct, the WRF manages to capture a similar transition in phase partitioning and can provide useful context for the observed transition.

A more detailed comparison of observed and simulated LWP and IWP is considered in Figs. 5a and 5b, respectively. Figure 5a shows that WRF-simulated LWP on 11 March is much lower than the MWR-derived LWP, while on 12 March their magnitude is similar. The underestimation of simulated cloud liquid water during 11 March relative to the measurements is due to the underestimation of water vapor mixing ratio in the ECMWF operational analysis used to initialize the WRF in the region where the mixed-phase cloud forms. Simulated IWP is generally lower (higher) than the retrieved values on 11 (12) March (Fig. 5b). However, it should be kept in mind that in the WRF Model the ice + snow number

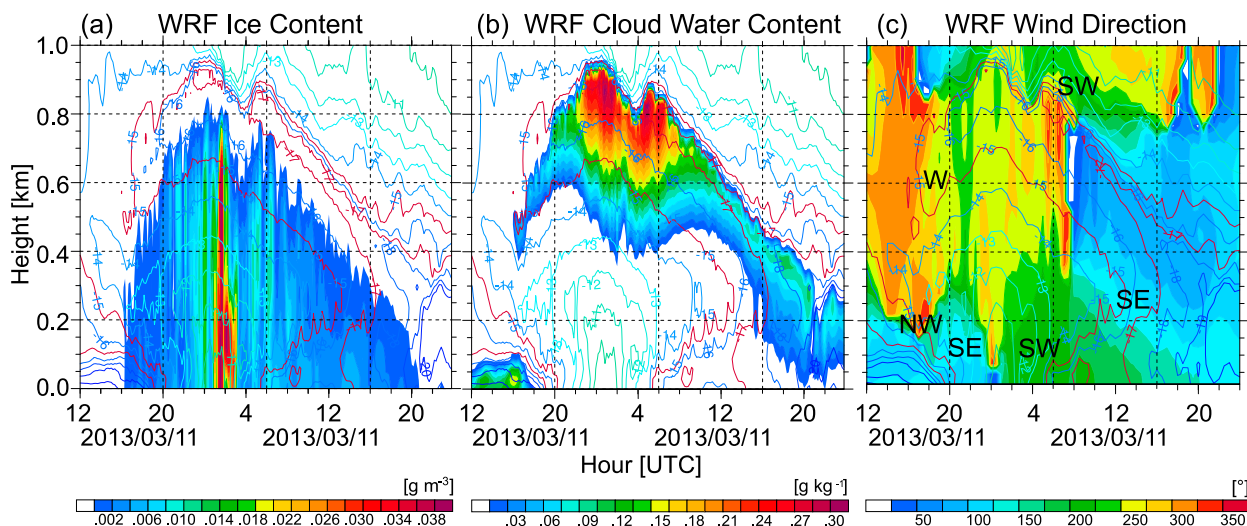


FIG. 9. Time-vs-height cross sections of WRF simulation results: (a) cloud + snow ice water content (IWC), (b) cloud liquid water content (LWC), and (c) wind direction (color shades) from the 0.3-km nest simulations. Contour lines in each panel represent temperature in $^{\circ}\text{C}$.

concentration are quasi-fixed since it is relaxed to 1 L^{-1} such that transitions in IN concentrations will not be represented. Instead, we should focus on what we can learn from the model in terms of phase partitioning evolution independently as done in Fig. 10.

Pulling information from both the observations and modeling results can help clarify details of the cloud transitions. As previously mentioned, the observations show a significant drop in IWP and retrieved N_{ice} concurrent with the change in wind direction and surface-coupling state. A similar picture is revealed from the WRF simulation results in Fig. 10a. The simulated IWP decreased after 0200 UTC 12 March, while simulated LWP remained high even as temperatures at the cloud base and below decreased (Fig. 10c). Given that LWC, cloud-base height, cloud-top height, and relative humidity (Fig. 10b) are similar before and after the passage of the snowbands, and that the cloud-level environment is cooling and in theory supporting additional production of ice (rather than the observed reduction), the fact that the phase partitioning between liquid and ice water content differs so dramatically in those two periods suggests a change in the availability of ice nucleating particles (IN) when the air mass change happened. However, since the given observations do not include profiles of IN, and the WRF Model uses a quasi-fixed N_{ice} , we are not able to fully explore this hypothesis.

WRF simulations suggest that particle residence time, and thus ice particle growth and size, may have played a key role in the transition in phase partitioning. Figure 10 additionally shows time series of vertical air motion w (positive = upward), mass-weighted mean

snowfall speed v (positive = downward), snow mixing ratio, snow number concentration, snow effective radius, and snow deposition rate, all averaged between cloud base and 200 m below cloud base where snow growth rates are largest. The focus here is on the description of snow because it comprises the majority of the frozen hydrometeor mass and the depletion of water vapor by deposition, which in turn determines how much water vapor is available for liquid formation. Figure 10d shows that the rapid increase in modeled IWP occurs when the vertical air velocity is upward and exceeds the fall speed of snow. The rapid decrease in modeled IWP occurs when the vertical motion weakens and is significantly less than the fall speed of snow. Interestingly, the LWP is relatively insensitive to the vertical velocity variability [consistent with previous studies such as Solomon et al. (2009)]. Therefore, the variability in modeled IWP can be understood in terms of the residence time of the snow crystals in the mixed layer, which decreases when the updrafts weaken (Yang et al. 2015).

In the model, the snow-effective radius only depends on the mass mixing ratio and number concentration of snow. Since the number concentration is essentially fixed, this means that variability of snow-effective radius (Fig. 10f) is essentially controlled by the variability of mass mixing ratio (Fig. 10e) alone. Mass mixing ratio is in turn affected by residence time and snow deposition rate (Fig. 10e). Observation-based retrieved values of D_{ge} were indeed found to be significantly larger during the time of strong ice precipitation compared to later on (Fig. 5e). However, retrieved N_{ice} is also higher during the period with increased precipitation (Fig. 5d). Thus,

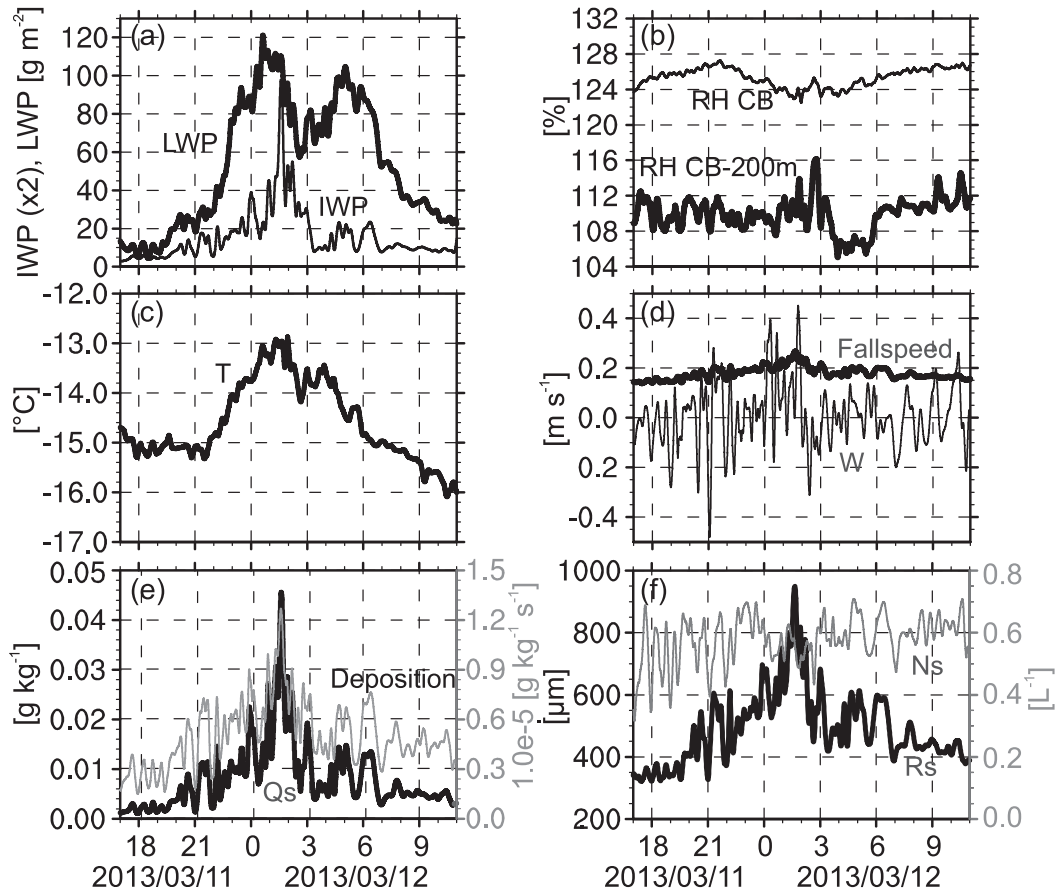


FIG. 10. The 10-min running mean time series of WRF simulation results: (a) LWP (thick line) and IWP ($\times 2$, thin line), units of g m^{-2} ; (b) relative humidity (%) with respect to ice at cloud base (thin line) and 200 m below cloud base (thick line); (c) temperature ($^{\circ}\text{C}$); (d) vertical velocity (thin line, positive = upward) and mass-weighted mean snowfall speed (thick line, positive = downward), in units of m s^{-1} ; (e) snow mixing ratio (thick black line), in units of g kg^{-1} , and snow deposition rate (thin gray line), in units of $10^{-5} \text{g kg}^{-1} \text{s}^{-1}$; and (f) snow effective radius (thick black line), in units of μm , and snow number concentration (thin gray line), in units of L^{-1} . Fields in (c)–(f) averaged from cloud base to 200 m below cloud base.

the variability of D_{ge} seems not be due to residence time variability only.

The potential radiative impacts of an upper-level cloud and changing solar input on the transition are also explored. Figure 11 shows the vertical profiles of cloud fraction, ice, and liquid for 12 March at 0600 and 1200 UTC. Using this information, radiative transfer calculations were completed to evaluate the impact of the upper-level cloud. Included in these are sensitivity tests that vary assumptions used to prescribe the IWC in the upper-level cloud, including varying this quantity within the range that includes the hourly mean (centered around 0600 and 1200 UTC, respectively) of the KAZR-derived IWC, the mean ± 1 standard deviation, and the observed maximum in the hour-long period. As an extreme scenario, the cirrus is neglected entirely. To conduct the radiative transfer simulations, in-cloud IWC is

converted into gridbox mean IWC using the KAZR-derived cloud fraction estimate before providing the input to the model.

These radiative transfer experiments were completed to determine to what extent the cirrus and the solar cycle may have impacted stratiform cloud-top cooling-driven turbulence in the boundary layer. The cloud-top cooling rate of the low-level cloud and its reduction due to the shading by the upper-level cloud (relative to the case without upper-level cloud) is shown in Fig. 11 (columns 4 and 5). The longwave cooling at cloud top of the liquid cloud is on the order of 56K day^{-1} at 0600 UTC (60K day^{-1} at 1200 UTC) if the upper-level cloud is neglected entirely. This cooling is reduced by $6\text{--}8 \text{K day}^{-1}$ if we assume IWC values in the upper cloud ranging between the hourly mean ± 1 standard deviation. Even when assuming that the upper-level cloud

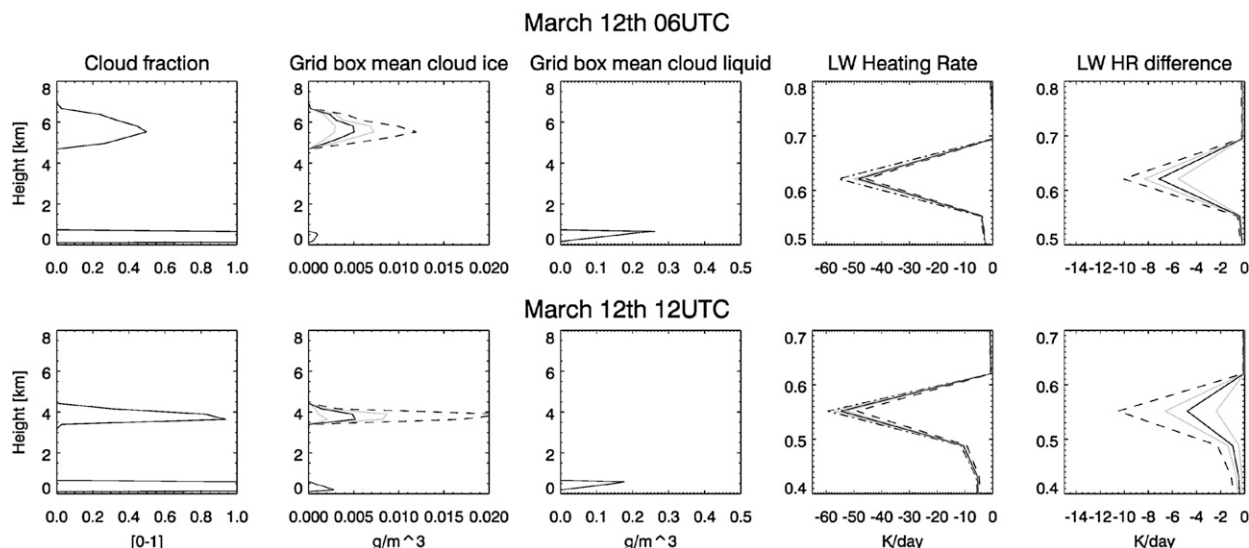


FIG. 11. Profiles of cloud fraction and gridbox mean ice water content (IWC) and liquid water content (LWC) derived from observations and prescribed for the radiation calculations at 0600 and 1200 UTC 12 Mar. In the IWC panels, the hourly mean (black solid) ± 1 standard deviation (solid gray) and maximum values (dashed black) derived from the KAZR retrieval are shown. In column 4, the resulting longwave (LW) heating rate at the top of the low-level mixed-phase cloud are shown for the various assumed IWC values, as well as for the case where the upper-level cloud is neglected (dash-dotted curve). In column 5, the change in the LW cloud-top heating rate relative to the no-cloud scenario is shown (no-cloud experiment).

contains the maximum observed value of IWC for the period of interest, cloud top cooling is reduced by only 10 K day^{-1} . Thus the cloud-top cooling may be reduced at most by 20%, but more likely by around 10%. To determine the potential influence of shortwave radiation on the mixed-phase cloud, the radiative heating profiles were calculated for noontime conditions (0000 UTC 12 March) applied to the same cloud profiles (no upper-level cloud) shown in Fig. 11. This resulted in a maximum shortwave heating rate on the order of $3\text{--}4 \text{ K day}^{-1}$ near cloud top. Thus, the shortwave heating rate at maximum solar zenith angle (SZA) of 15° is comparable or somewhat smaller in magnitude than the change in longwave cooling due to the upper-level ice cloud. We can conclude that, while the solar cycle or shielding by the upper-level cloud may well modulate the strength of cloud-top cooling driven turbulence in the boundary layer [as in Shupe et al. (2013)], it is unlikely that the appearance of the cirrus leads to a significant shift in the boundary layer turbulent structure and the associated dynamics within the lower cloud layer.

6. Summary

A low-level mixed-phase stratiform cloud case from Barrow, Alaska, is examined in great detail using a sophisticated observational suite and multiple modeling perspectives to determine key processes that control transitions in cloud phase partitioning. Evidence suggests

that three main factors contributed to the abrupt change in phase partitioning for this case. First, the large-scale advection of different air masses with different moisture content and indications of different aerosol concentrations played a role. During the time of highest ice and liquid water contents, the air mass over Barrow had a relatively high aerosol concentration and was supported by moist advection at cloud level. Additional moisture for the cloud system may have been provided to the air mass from the nearby open area of Arctic Ocean. This moisture advection helped to support cloud persistence on 11 March, but was eventually replaced by drier southeasterly flow. This airmass transition, which followed a mesoscale boundary with warm-front characteristics at 2300 UTC 11 March, was characterized by a reduced aerosol load as well as decreasing cloud and surface temperatures and decreasing water vapor supply. Second, cloud-scale processes, specifically the cloud-surface thermodynamic coupling state, changed at the time of this airmass transition. Prior to the transition a higher IWP was maintained when the cloud was decoupled from the surface with a relatively dry near-surface layer below the cloud. This structure may have supported subcloud sublimation for ice crystals such that IN were not lost to the surface and may have continued to be available to the cloud via IN recycling. After the transition the cloud became coupled to the near surface with high levels of moisture extending down to the surface. As a result precipitating ice,

including the limited supply of IN, was lost from the cloud system to the surface. Third, WRF simulations suggest that the residence time of ice particles, which is linked to local-scale dynamics, was also important in the change of phase partitioning. Simulated IWP was found to be higher during times of strong updrafts that dominated during the early part of the case. After the transition, updrafts weakened and ice crystals fell more quickly from the cloud system. The radiative shielding of a cirrus on 12 March as well as the influence of the solar cycle were found to be of minor importance for turbulence modulation in the mixed-phase cloud, and thus likely did not play key roles in the transition.

In conclusion, this study brings together a unique variety of observations and modeling approaches that help to shed light on processes important for phase partitioning, including both cloud-scale processes and large-scale environmental forcings. While retrievals of additional parameters such as particle fall speeds and precipitation fluxes could be useful to support enhanced analyses (Bühl et al. 2016), a lack of observations of aerosol properties, including IN concentrations and vertical profiles of aerosol particle concentrations and size, pose a large challenge for understanding phase transitions. As highlighted by Paramonov et al. (2015) the accurate connection between available CCN and cloud droplet number concentration as well as available IN and ice particle number concentration can only be made via better sampling of these key parameters. Ultimately, such observations are needed to unravel the role of aerosol–cloud interactions in driving transitions in cloud phase partitioning. Additionally, this study suggests that the interplay of aerosol-induced cloud microphysical properties with cloud dynamic and thermodynamic processes may also be critically important.

While the WRF simulations included in this study were able to reproduce the large-scale dynamical forcing for this case, some microphysical interpretations were hampered due to model limitations in representing aerosol–cloud interactions and their influence on microphysics. Ultimately improved observation and representation of these processes will be needed to develop models that can successfully characterize cloud phase.

Acknowledgments. Thanks to Janek Zimmer for help in analyzing the synoptic situation and to Kara Sulia as well as Stefan Kneifel for fruitful discussions in the early phase of this case study analysis. All remote-sensing data is from the ARM data archive. Soundings at 0000 and 1200 UTC are from the National Weather Service in Barrow, the remaining ones are from the ARM data archive. Aerosol measurements are provided and

supported by the NOAA/Global Monitoring Division (GMD). The authors gratefully acknowledge the NOAA/Air Resources Laboratory (ARL) for the provision of the HYSPLIT transport and dispersion model and the READY website (<http://www.ready.noaa.gov>) used in this publication. The High Spectral Resolution Lidar data in Fig. 1 were obtained from the University of Wisconsin Lidar Group homepage (<http://lidar.ssec.wisc.edu/index.htm>). H. Kalesse conducted this study within the framework of the DFG project COMPoSE, GZ: KA 4162/1-1. G. de Boer contributed to this research under funding from the U.S. Department of Energy's (DOE's) Atmospheric System Research (ASR) program (Projects: DE-SC0008794 and DE-SC0013306) as well as the U.S. National Science Foundation (ARC 1203902). M. Shupe was supported by DOE-ASR Grant DE-SC0011918. M. Ahlgrimm's contribution to this work was supported by DOE-ASR Grant DE-SC0005259. Furthermore, this research was also supported in part under DOE ASR Grant DE-SC00112704 (E. Luke), DE-SC0013953 (M. Oue), DE-SC0006974 (D. Zhang), and DE-SC0014239 (D. Zhang).

REFERENCES

- Abdul-Razzak, H., and S. J. Ghan, 2000: A parameterization of aerosol activation. 2, Multiple aerosol types. *J. Geophys. Res.*, **105**, 6837–6844, doi:10.1029/1999JD901161.
- Barker, H., R. Pincus, and J.-J. Morcrette, 2002: The Monte-Carlo independent column approximation: Application within large-scale models. *Proc. GCSS/ARM Workshop on the Representation of Cloud Systems in Large-Scale Models*, Kananaskis, AB, Canada, 10 pp. [Available online at <http://www.met.utah.edu/skrueger/gcss-2002/Extended-Abstracts.pdf>.]
- Benedetti, A., and Coauthors, 2009: Aerosol analysis and forecast in the European Centre for Medium-Range Weather Forecasts Integrated Forecast System: 2. Data assimilation. *J. Geophys. Res.*, **114**, D13205, doi:10.1029/2008JD011115.
- Bergeron, T., 1935: On the physics of clouds and precipitation. *Proces Verbaux de l'Association de Meteorologie*, P. Duport, Ed., International Union of Geodesy and Geophysics, 156–178.
- Brown, J., and V. Romanovsky, 2008: Report from the international permafrost association: State of permafrost in the first decade of the 21st century. *Permafr. Periglac. Processes*, **19**, 255–260, doi:10.1002/ppp.618.
- Browning, K. A., and R. Wexler, 1968: The determination of kinematic properties of a wind field using Doppler radar. *J. Appl. Meteor.*, **7**, 105–113, doi:10.1175/1520-0450(1968)007<0105:TDOKPO>2.0.CO;2.
- Bühl, J., P. Seifert, A. Myagkov, and A. Ansmann, 2016: Measuring ice- and liquid-water properties in mixed-phase cloud layers at the Leipzig Cloudnet station. *Atmos. Chem. Phys.*, **16**, 10 609–10 620, doi:10.5194/acp-16-10609-2016.
- Cadeddu, M. P., J. C. Liljegren, and D. D. Turner, 2013: The Atmospheric Radiation Measurement (ARM) program network of microwave radiometers: Instrumentation, data, and retrievals. *Atmos. Meas. Tech.*, **6**, 2359–2372, doi:10.5194/amt-6-2359-2013.

- Chapman, W. L., and J. E. Walsh, 1993: Recent variations of sea ice and air temperature in high latitudes. *Bull. Amer. Meteor. Soc.*, **74**, 33–47, doi:10.1175/1520-0477(1993)074<0033:RVOSIA>2.0.CO;2.
- Chen, F., and J. Dudhia, 2001: Coupling an advanced land surface-hydrology model with the Penn State–NCAR MM5 modeling system. Part I: Model implementation and sensitivity. *Mon. Wea. Rev.*, **129**, 569–585, doi:10.1175/1520-0493(2001)129<0569:CAALSH>2.0.CO;2.
- Collins, W. D., and Coauthors, 2004: Description of the NCAR Community Atmosphere Model (CAM 3.0). NCAR Tech. Note NCAR/TN-464+STR, NCAR, 214 pp. [Available online at <http://www.cesm.ucar.edu/models/atm-cam/docs/description/description.pdf>.]
- Comiso, J., 2012: Large decadal decline of the arctic multi-year ice cover. *J. Climate*, **25**, 1176–1193, doi:10.1175/11-00113.1.
- , C. Parkinson, R. Gersten, and L. Stock, 2008: Accelerated decline in the Arctic sea ice cover. *Geophys. Res. Lett.*, **35**, L01703, doi:10.1029/2007GL031972.
- de Boer, G., E. Eloranta, and M. Shupe, 2009: Arctic mixed-phase stratiform cloud properties from multiple years of surface-based measurements at two high-latitude locations. *J. Atmos. Sci.*, **66**, 2874–2887, doi:10.1175/2009JAS3029.1.
- , W. Chapman, J. Kay, B. Medeiros, M. Shupe, S. Vavrus, and J. Walsh, 2012: A characterization of the present-day Arctic atmosphere in CCSM4. *J. Climate*, **25**, 2676–2695, doi:10.1175/JCLI-D-11-00228.1.
- , and Coauthors, 2014: Near-surface meteorology during the Arctic Summer Cloud Ocean Study (ASCOS): Evaluation of reanalyses and global climate models. *Atmos. Chem. Phys.*, **14**, 427–445, doi:10.5194/acp-14-427-2014.
- Draxler, R., and G. Hess, 1998: An overview of the HYSPLIT4 modeling system of trajectories, dispersion, and deposition. *Aust. Meteor. Mag.*, **47**, 295–308.
- , and G. Rolph, 2015: HYSPLIT (Hybrid Single-Particle Lagrangian Integrated Trajectory) model access via NOAA ARL ready website. NOAA/Air Resources Laboratory, Silver Spring, MD, accessed 2 February 2016. [Available online at <http://ready.arl.noaa.gov/HYSPLIT.php>.]
- Dupont, J.-C., and Coauthors, 2010: Macrophysical and optical properties of midlatitude cirrus clouds from four ground-based lidars and collocated CALIOP observations. *J. Geophys. Res.*, **115**, D00H24, doi:10.1029/2009JD011943.
- Dyer, A. J., and B. B. Hicks, 1970: Flux-gradient relationships in the constant flux layer. *Quart. J. Roy. Meteor. Soc.*, **96**, 715–721, doi:10.1002/qj.49709641012.
- Eloranta, E., 2005: High spectral resolution lidar. *Lidar: Range-Resolved Optical Remote-Sensing of the Atmosphere*, K. Weitkamp, Ed., Springer-Verlag, 143–164.
- English, J., A. Gettelman, and G. Henderson, 2015: Arctic radiative fluxes: Present-day biases and future projections in CMIP5 models. *J. Climate*, **28**, 6019–6038, doi:10.1175/JCLI-D-14-00801.1.
- Fan, J., M. Ovtchinnikov, J. M. Comstock, S. A. McFarlane, and A. Khain, 2009: Ice formation in Arctic mixed-phase clouds: Insights from a 3-D cloud-resolving model with size-resolved aerosol and cloud microphysics. *J. Geophys. Res.*, **114**, D04205, doi:10.1029/2008JD010782.
- Findeisen, W., 1938: Kolloid-meteorologische Vorgänge bei Niederschlagsbildung. *Meteor. Z.*, **55**, 121–133.
- Fridlind, A. M., B. van Dierenhoven, A. S. Ackerman, A. Avramov, A. Mrowiec, H. Morrison, P. Zuidema, and M. D. Shupe, 2012: A FIRE-ACE/SHEBA case study of mixed-phase Arctic boundary layer clouds: Entrainment rate limitations on rapid primary ice nucleation processes. *J. Atmos. Sci.*, **69**, 365–389, doi:10.1175/JAS-D-11-052.1.
- Fu, Q., 1996: An accurate parameterization of the solar radiative properties of cirrus clouds for climate models. *J. Climate*, **9**, 2058–2082, doi:10.1175/1520-0442(1996)009<2058:AAPOTS>2.0.CO;2.
- Fukuta, N., and T. Takahashi, 1999: The growth of atmospheric ice crystals: A summary of findings in vertical supercooled cloud tunnel studies. *J. Atmos. Sci.*, **56**, 1963–1979, doi:10.1175/1520-0469(1999)056<1963:TGOAIC>2.0.CO;2.
- Hansen, J., R. Ruedy, M. Sato, and K. Lo, 2010: Global surface temperature change. *Rev. Geophys.*, **48**, RG4004, doi:10.1029/2010RG000345.
- Harrington, J., T. Reisin, W. Cotton, and S. Kreidenweis, 1999: Cloud resolving simulations of Arctic stratus. Part II: Transition-season clouds. *Atmos. Res.*, **51**, 45–75, doi:10.1016/S0169-8095(98)00098-2.
- Heymsfield, A. J., and Coauthors, 2008: Testing IWC retrieval methods using radar and ancillary measurements with in situ data. *J. Appl. Meteor. Climatol.*, **47**, 135–163, doi:10.1175/2007JAMC1606.1.
- Hogan, R. J., M. P. Mittermaier, and A. J. Illingworth, 2006: The retrieval of ice water content from radar reflectivity factor and temperature and its use in evaluating a mesoscale model. *J. Appl. Meteor. Climatol.*, **45**, 301–317, doi:10.1175/JAM2340.1.
- Hong, S., Y. Noh, and J. Dudhia, 2006: A new vertical diffusion package with an explicit treatment of entrainment processes. *Mon. Wea. Rev.*, **134**, 2318–2341, doi:10.1175/MWR3199.1.
- Illingworth, A. J., and Coauthors, 2007: Cloudnet: Continuous evaluation of cloud profiles in seven operational models using ground-based observations. *Bull. Amer. Meteor. Soc.*, **88**, 883–898, doi:10.1175/BAMS-88-6-883.
- Intrieri, J., C. Fairall, M. Shupe, P. Persson, E. Andreas, P. Guest, and R. Moritz, 2002: An annual cycle of Arctic surface cloud forcing at SHEBA. *J. Geophys. Res.*, **107**, 8039, doi:10.1029/2000JC000439.
- Kalesse, H., W. Szyrmer, S. Kneifel, P. Kollias, and E. Luke, 2016: Fingerprints of a riming event on cloud radar Doppler spectra: Observations and modeling. *Atmos. Chem. Phys.*, **16**, 2997–3012, doi:10.5194/acp-16-2997-2016.
- Kay, J., and A. Gettelman, 2009: Cloud influence on and response to seasonal Arctic sea ice loss. *J. Geophys. Res.*, **114**, D18204, doi:10.1029/2009JD011773.
- , T. L'Ecuyer, A. Gettelman, G. Stephens, and C. O'Dell, 2008: The contribution of cloud and radiation anomalies to the 2007 Arctic sea ice extent minimum. *Geophys. Res. Lett.*, **35**, L08503, doi:10.1029/2008GL033451.
- Klein, S., and Coauthors, 2009: Intercomparison of model simulations of mixed-phase clouds observed during the ARM Mixed-Phase Arctic Cloud Experiment. Part I: Single-layer cloud. *Quart. J. Roy. Meteor. Soc.*, **135**, 979–1002, doi:10.1002/qj.416.
- Kollias, P., M. A. Miller, E. P. Luke, K. L. Johnson, E. E. Clothiaux, K. P. Moran, K. B. Widener, and B. A. Albrecht, 2007: The atmospheric radiation measurement program cloud profiling radars. *J. Atmos. Oceanic Technol.*, **24**, 1199–1214, doi:10.1175/JTECH2033.1.
- Luke, E. P., P. Kollias, and M. D. Shupe, 2010: Detection of supercooled liquid in mixed-phase clouds using radar Doppler spectra. *J. Geophys. Res.*, **115**, D19201, doi:10.1029/2009JD012884.
- McFarquhar, G. M., and Coauthors, 2011: Indirect and semi-direct aerosol campaign: The impact of Arctic aerosols on clouds.

- Bull. Amer. Meteor. Soc.*, **92**, 183–201, doi:10.1175/2010BAMS2935.1.
- Miller, G. H., S. Lehman, K. A. Refsnider, J. R. Southon, and Y. Zhong, 2013: Unprecedented recent summer warmth in Arctic Canada. *Geophys. Res. Lett.*, **40**, 5745–5751, doi:10.1002/2013GL057188.
- Mlawer, E., S. Taubman, P. Brown, M. Iacono, and S. Clough, 1997: Radiative transfer for inhomogeneous atmospheres: RRTM, a validated correlated-k model for the longwave. *J. Geophys. Res.*, **102**, 16 663–16 682, doi:10.1029/97JD00237.
- Morcrette, J.-J., H. W. Barker, J. N. S. Cole, M. J. Iacono, and R. Pincus, 2008: Impact of a new radiation package, McRad, in the ECMWF Integrated Forecasting System. *Mon. Wea. Rev.*, **136**, 4773–4798, doi:10.1175/2008MWR2363.1.
- , and Coauthors, 2009: Aerosol analysis and forecast in the European Centre for Medium-Range Weather Forecasts Integrated Forecast System: Forward modeling. *J. Geophys. Res.*, **114**, D06206, doi:10.1029/2008JD011235.
- Morrison, H., and J. O. Pinto, 2005: Mesoscale modeling of springtime Arctic mixed-phase stratiform clouds using a new two-moment bulk microphysics scheme. *J. Atmos. Sci.*, **62**, 3683–3704, doi:10.1175/JAS3564.1.
- , G. Thompson, and V. Tatarskii, 2009: Impact of cloud microphysics on the development of trailing stratiform precipitation in a simulated squall line: Comparison of one- and two-moment schemes. *Mon. Wea. Rev.*, **137**, 991–1007, doi:10.1175/2008MWR2556.1.
- , and Coauthors, 2011: Intercomparison of cloud model simulations of Arctic mixed-phase boundary layer clouds observed during SHEBA/FIRE-ACE. *J. Adv. Model. Earth Syst.*, **3**, M05001, doi:10.1029/2011MS000066.
- , G. de Boer, G. Feingold, J. Harrington, M. Shupe, and K. Sulia, 2012: Resilience of persistent Arctic mixed-phase clouds. *Nat. Geosci.*, **5**, 11–17, doi:10.1038/ngeo1332.
- Oue, M., M. Galletti, J. Verlinde, A. Ryzhkov, and Y. Lu, 2016: Use of X-band differential reflectivity measurements to study shallow Arctic mixed-phase clouds. *J. Appl. Meteor. Climatol.*, **55**, 403–424, doi:10.1175/JAMC-D-15-0168.1.
- Ovchinnikov, M., and Coauthors, 2014: Intercomparison of large-eddy simulations of Arctic mixed-phase clouds: Importance of ice size distribution assumptions. *J. Adv. Model. Earth Syst.*, **6**, 223–248, doi:10.1002/2013MS000282.
- Paramonov, M., and Coauthors, 2015: A synthesis of cloud condensation nuclei counter (CCNC) measurements within the EUCAARI network. *Atmos. Chem. Phys.*, **15**, 12 211–12 229, doi:10.5194/acp-15-12211-2015.
- Paulson, C. A., 1970: The mathematical representation of wind speed and temperature profiles in the unstable atmospheric surface layer. *J. Appl. Meteor.*, **9**, 857–861, doi:10.1175/1520-0450(1970)009<0857:TMROWS>2.0.CO;2.
- Pincus, R., H. Barker, and J.-J. Morcrette, 2003: A fast, flexible, approximate technique for computing radiative transfer in inhomogeneous cloud fields. *J. Geophys. Res.*, **108**, 4376, doi:10.1029/2002JD003322.
- Protat, A., D. Bouniol, E. J. O'Connor, H. Klein Baltink, J. Verlinde, and K. Widener, 2011: *CloudSat* as a global radar calibrator. *J. Atmos. Oceanic Technol.*, **28**, 445–452, doi:10.1175/2010JTECHA1443.1.
- Przybylak, R., 2007: Recent air-temperature changes in the Arctic. *Ann. Glaciol.*, **46**, 316–324, doi:10.3189/172756407782871666.
- Rolph, G., 2016: READY—Real-time Environmental Applications and Display sYstem website. NOAA/Air Resources Laboratory, College Park, MD, accessed 2 February 2016. [Available online at <http://www.ready.noaa.gov>.]
- Romanovsky, V., M. Burgess, S. Smith, K. Yoshikawa, and J. Brown, 2002: Permafrost temperature records: Indicators of climate change. *Eos, Trans. Amer. Geophys. Union*, **83**, 589–594, doi:10.1029/2002EO000402.
- Sassen, K., 2005: Polarization in lidar. *Lidar: Range-Resolved Optical Remote-Sensing of the Atmosphere*, K. Weitkamp, Ed., Springer-Verlag, 19–42.
- Savre, J., A. M. L. Ekman, G. Svensson, and M. Tjernström, 2015: Large-eddy simulations of an Arctic mixed-phase stratiform cloud observed during ISDAC: Sensitivity to moisture aloft, surface fluxes and large-scale forcing. *Quart. J. Roy. Meteor. Soc.*, **141**, 1177–1190, doi:10.1002/qj.2425.
- Schweiger, A., R. Lindsay, S. Vavrus, and J. Francis, 2008: Relationships between Arctic sea ice and clouds during autumn. *J. Climate*, **21**, 4799–4810, doi:10.1175/2008JCLI2156.1.
- Sedlar, J., M. D. Shupe, and M. Tjernström, 2012: On the relationship between thermodynamic structure and cloud top, and its climate significance in the Arctic. *J. Climate*, **25**, 2374–2393, doi:10.1175/JCLI-D-11-00186.1.
- Serreze, M., and R. Barry, 2011: Processes and impacts of Arctic amplification: A research synthesis. *Global Planet. Change*, **77**, 85–96, doi:10.1016/j.gloplacha.2011.03.004.
- , A. Barrett, J. Stroeve, D. Kindig, and M. Holland, 2009: The emergence of a surface-based Arctic amplification. *Cryosphere*, **3**, 11–19, doi:10.5194/tc-3-11-2009.
- Shupe, M. D., 2007: A ground-based multisensor cloud phase classifier. *Geophys. Res. Lett.*, **34**, L22809, doi:10.1029/2007GL031008.
- , 2011: Clouds at Arctic atmospheric observatories. Part II: Thermodynamic phase characteristics. *J. Appl. Meteor. Climatol.*, **50**, 645–661, doi:10.1175/2010JAMC2468.1.
- , and J. Intrieri, 2004: Cloud radiative forcing of the Arctic surface: The influence of cloud properties, surface albedo, and solar zenith angle. *J. Climate*, **17**, 616–628, doi:10.1175/1520-0442(2004)017<0616:CRFOTA>2.0.CO;2.
- , P. Kollias, S. Matrosov, and T. Schneider, 2004: Deriving mixed-phase cloud properties from Doppler radar spectra. *J. Atmos. Oceanic Technol.*, **21**, 660–670, doi:10.1175/1520-0426(2004)021<0660:DMCPFD>2.0.CO;2.
- , S. Y. Matrosov, and T. Uttal, 2006: Arctic mixed-phase cloud properties derived from surface-based sensors at SHEBA. *J. Atmos. Sci.*, **63**, 697–711, doi:10.1175/JAS3659.1.
- , P. Kollias, M. Poellot, and E. Eloranta, 2008: On deriving vertical air motions from cloud radar Doppler spectra. *J. Atmos. Oceanic Technol.*, **25**, 547–557, doi:10.1175/2007JTECHA1007.1.
- , I. Brooks, and G. Canut, 2012: Evaluation of turbulent dissipation rate retrievals from Doppler cloud radar. *Atmos. Meas. Tech.*, **5**, 1375–1385, doi:10.5194/amt-5-1375-2012.
- , P. O. G. Persson, I. M. Brooks, M. Tjernström, J. Sedlar, T. Mauritsen, S. Sjogren, and C. Leck, 2013: Cloud and boundary layer interactions over the Arctic sea ice in late summer. *Atmos. Chem. Phys.*, **13**, 9379–9399, doi:10.5194/acp-13-9379-2013.
- , D. Turner, A. Zwink, M. Thieman, E. Mlawer, and T. Shippert, 2015: Deriving Arctic cloud microphysics at Barrow, Alaska: Algorithms, results, and Radiative closure. *J. Appl. Meteor. Climatol.*, **54**, 1675–1689, doi:10.1175/JAMC-D-15-0054.1.
- Solomon, A., H. Morrison, P. Persson, M. Shupe, and J.-W. Bao, 2009: Investigation of microphysical parameterizations of snow and ice in Arctic clouds during M-PACE through model-observation comparisons. *Mon. Wea. Rev.*, **137**, 3110–3128, doi:10.1175/2009MWR2688.1.

- , M. Shupe, P. Persson, and H. Morrison, 2011: Moisture and dynamical interactions maintaining decoupled Arctic mixed-phase stratocumulus in the presence of a humidity inversion. *Atmos. Chem. Phys.*, **11**, 10 127–10 148, doi:10.5194/acp-11-10127-2011.
- , O. Persson, H. Morrison, T. Yamaguchi, P. Caldwell, and G. deBoer, 2014: The sensitivity of springtime Arctic mixed-phase stratocumulus clouds to surface-layer and cloud-top inversion-layer moisture sources. *J. Atmos. Sci.*, **71**, 574–595, doi:10.1175/JAS-D-13-0179.1.
- , G. Feingold, and M. Shupe, 2015: The role of ice nuclei recycling in the maintenance of cloud ice in Arctic mixed-phase stratocumulus. *Atmos. Chem. Phys.*, **15**, 10 631–10 643, doi:10.5194/acp-15-10631-2015.
- Sotiropoulou, G., J. Sedlar, M. Tjernström, M. D. Shupe, I. M. Brooks, and P. O. G. Persson, 2014: The thermodynamic structure of summer Arctic stratocumulus and the dynamic coupling to the surface. *Atmos. Chem. Phys.*, **14**, 12 573–12 592, doi:10.5194/acp-14-12573-2014.
- Stroeve, J., M. Holland, W. Meier, T. Scambos, and M. Serreze, 2007: Arctic sea ice decline: Faster than forecast. *Geophys. Res. Lett.*, **34**, L09501, doi:10.1029/2007GL029703.
- Tjernström, M., J. Sedlar, and M. D. Shupe, 2008: How well do regional climate models reproduce radiation and clouds in the Arctic? An evaluation of ARCMIP simulations. *J. Appl. Meteor. Climatol.*, **47**, 2405–2422, doi:10.1175/2008JAMC1845.1.
- Verlinde, J., and Coauthors, 2007: The Mixed-Phase Arctic Cloud Experiment. *Bull. Amer. Meteor. Soc.*, **88**, 205–221, doi:10.1175/BAMS-88-2-205.
- , M. P. Rambukkange, E. E. Clothiaux, G. M. McFarquhar, and E. W. Eloranta, 2013: Arctic multilayered, mixed-phase cloud processes revealed in millimeter-wave cloud radar Doppler spectra. *J. Geophys. Res. Atmos.*, **118**, 13 199–13 213, doi:10.1002/2013JD020183.
- , B. D. Zak, M. D. Shupe, M. D. Ivey, and K. Stamnes, 2016: The ARM North Slope of Alaska (NSA) sites. *The Atmospheric Radiation Measurement Program: The First 20 Years*, Meteor. Monogr., No. 57, Amer. Meteor. Soc., 8.1–8.13, doi:10.1175/AMSMONOGRAPHS-D-15-0023.1.
- Wang, Z., and K. Sassen, 2002: Cirrus cloud microphysical property retrieval using lidar and radar measurements. Part I: Algorithm description and comparison with in situ data. *J. Appl. Meteor.*, **41**, 218–229, doi:10.1175/1520-0450(2002)041<0218:CCMPRU>2.0.CO;2.
- , T. Luo, D. Zhang, and J. Snider, 2014: Lidar based cloud droplet concentration retrieval in supporting aerosol-cloud interaction study in low clouds. *Fifth Atmospheric System Research (ASR) Science Team Meeting*, Potomac, MD, U.S. Department of Energy, Office of Biological and Environmental Research. [Available online at <http://asr.science.energy.gov/meetings/stm/2014/presentations/Low-cloud-N.pdf>.]
- Webb, E. K., 1970: Profile relationships: The log-linear range, and extension to strong stability. *Quart. J. Roy. Meteor. Soc.*, **96**, 67–90, doi:10.1002/qj.49709640708.
- Wegener, A., 1911: *Thermodynamik der Atmosphäre*. Leipzig, 331 pp.
- Westwater, E. R., Y. Han, M. D. Shupe, and S. Y. Matrosov, 2001: Analysis of integrated cloud liquid and precipitable water vapor retrievals from microwave radiometers during SHEBA. *J. Geophys. Res.*, **106**, 32 019–32 030, doi:10.1029/2000JD000055.
- Yang, F., M. Ovchinnikov, and R. Shaw, 2015: Long-lifetime ice particles in mixed-phase stratiform clouds: Quasi-steady and recycled growth. *J. Geophys. Res. Atmos.*, **120**, 11 617–11 635, doi:10.1002/2015JD023679.
- Yu, G., J. Verlinde, E. E. Clothiaux, and Y.-S. Chen, 2014: Mixed-phase cloud phase partitioning using millimeter wavelength cloud radar Doppler velocity spectra. *J. Geophys. Res. Atmos.*, **119**, 7556–7576, doi:10.1002/2013JD021182.
- Zhang, D., and R. Anthes, 1982: A high resolution model of the planetary boundary layer sensitivity tests and comparisons with SESAME79 data. *J. Appl. Meteor.*, **21**, 1594–1609, doi:10.1175/1520-0450(1982)021<1594:AHRMOT>2.0.CO;2.
- , W. Wang, A. Heymsfield, J. Fan, and T. Luo, 2014: Ice concentration retrieval in stratiform mixed-phase clouds using cloud radar reflectivity measurements and 1D ice growth model simulations. *J. Atmos. Sci.*, **71**, 3613–3635, doi:10.1175/JAS-D-13-0354.1.